Optical Sensing by Metamaterials and Metasurfaces: From Physics to Biomolecule Detection

Sayed Ali Khan, Noor Zamin Khan, Yinong Xie, Muhammad Tahir Abbas, Muhammad Rauf, Ikhtisham Mehmood, Marcin Runowski, Simeon Agathopoulos, and Jinfeng Zhu*

Metasurfaces are planar or 2D forms of metamaterials made up of arrays of antennas with a subwavelength thickness. They have been rapidly developed in the recent years due to their ability to manipulate light–matter interaction in both linear and non-linear regimes at the nanoscale. Various metasurfaces display remarkable optical features, such as acute resonance, significant near-field enhancement, and suitable capacity to support electric and magnetic modes, on account of the strong light–matter interaction and the low optical loss. Due to these important properties, they can be used in several advanced optoelectronic applications, like surface-enhanced spectroscopy, photo-catalysis, and sensing. This review reports on the recent progress of meta-materials and metasurfaces in molecular optical sensors. The principles that govern plasmonic and dielectric metasurfaces along with their features are outlined, supported by numerous examples. Then, the factors that result in a high Q-factor are presented in order to show that metamaterials and meta-surfaces can be used for label-free sensing in a variety of detection mecha-nisms, including surface-enhanced spectroscopy, refractometric sensing, and surface-enhanced thermal emission spectroscopy via infrared absorption and Raman scattering, as well as chiral sensing. Finally, the challenges for future development are outlined.

1. Introduction

Optical biosensors are a versatile detection and analysis tool used in biological research, health care, pharmaceuticals, environmental monitoring, homeland security, and the battlefield.[1] They do not interfere with electromagnetic (EM) radiation, manifest distant sensing capability, and may enable multiplexed detection in a single device. Optical biosensing technologies are widely used in current biomedical and environmental monitoring applications because they provide a reliable and quick way to identify and discriminate specific objects from a wide range of samples.[2–5] More interestingly, Optical biosensors outperform standard analytical techniques by delivering highly-sensitive, selective, and cost-effective real-time and label-free detection of biological and chemical molecules.[6,7] High specificities, sensitivity, small size, and cost-effectiveness are among the benefits.

S. A. Khan, Y. Xie, J. Zhu
School of Electronic Science and Engineering
Fujian Provincial Key Laboratory of Electromagnetic Wave Science and Detection Technology
Xiamen University
Xiamen 361005, P. R. China
E-mail: jfzhu@xmu.edu.cn

S. A. Khan
Hoffman Institute of Advanced Materials
Shenzhen Polytechnic 7098, Liuxian Blvd, Nanshan District
Shenzhen 5018055, P. R. China

N. Z. Khan
CAS Key Laboratory of Materials for Energy Conversion
School of Chemistry and Materials Science
University of Science and Technology of China
Hefei, Anhui 230026, P. R. China

M. T. Abbas
Key Laboratory of Strongly Coupled Quantum Matter Physics
Chinese Academy of Sciences
School of Physical Sciences
University of Science and Technology of China
No. 96 Jinzhai Road, Hefei, Anhui Province 230026, P. R. China

M. Rauf, I. Mehmood
College of Microscale Optoelectronics Engineering
Shenzhen University
Shenzhen 518060, P. R. China

M. Runowski
Departamento de Física
Universidad de La Laguna
Apartado de Correos 456, San Cristóbal de La Laguna,
Santa Cruz de Tenerife E-38200, Spain

M. Runowski
Faculty of Chemistry
Adam Mickiewicz University
Uniwersytetu Poznańskiego 8, Poznań 61-614, Poland

S. Agathopoulos
Department of Materials Science and Engineering
University of Ioannina
Ioannina GR-451 10, Greece

ADVANCED
SCIENCE NEWS
www.advancedsciencenews.com

ADVANCED
OPTICAL
MATERIALS
www.advopticalmat.de

The metasurface is a 2D variant of metamaterials that is often made up of an array of unit metal/dielectric nanostructure elements with specific sizes, shapes, and orientations. Metasurface research has gotten a lot of interest in recent years because of the growing demand for optical lenses, sensing, light trapping, integrated circuits, high-resolution imaging, chemical analysis, and photo-thermal manipulation.[7–9] Among them, the optical biosensing-based metasurfaces have achieved impressive results because of their capacity to confine light into nanoscale EM hotspots, which have been used to improve the sensitivity of various detection techniques effectively. Furthermore, this approach benefits nanoscale near-field enhancement with excellent sensitivity and non-destructive operation for high-throughput real-time detection.[4,10,11]

Plasmonic metasurfaces, for example, have made it possible to identify monolayers and their real-time interactions with biomolecules in the mid-infrared (IR) regime. It is a challenge to achieve identification via visualization with the aid of traditional IR absorption spectroscopy.[12–14] More specifically, metasurfaces can overcome the limitations of traditional terahertz (THz) spectroscopy by producing fine features equal to the size of the molecules or microorganisms. More interestingly, the metasurfaces are extremely sensitive to minute changes in the surrounding environment, allowing a more precise detection than traditional THz spectroscopy. Metallic nanostructures (such as Au, Ag, and Al) have been used extensively for biosensing, and various devices have been developed.[15–19] Various nanostructured metasurfaces have been introduced to improve the performance of plasmonic sensors, driven by the intense demand for quick, highly sensitive, and cost-effective biosensing for point-of-care diagnosis and mobile healthcare.[14,20,21] The development of low-cost, flexible, and disposable plasmonic metasurfaces with biomedical functionalization for high-performance biosensors are highly demanded practical applications. In our previous work,[22] we demonstrated the fabrication of low-cost flexible bio-functionalized plasmonic metasurfaces for high-sensitivity label-free tumor marker detection in human serum samples. More specifically, plasmonic metasurfaces with periodic gold nanobumps are created in a resist-free manner on a lightweight and flexible polycarbonate substrate that can be processed quickly using nanoimprint, etching, and metal evaporation. The proposed fabrication process reduces the weight and cost of the materials from 1.87 to 0.42 g (2-inch wafer) and from $6 to $0.85. The bulk sensitivity and quality factor (Q) of the manufactured low-cost plasmonic metasurfaces improved by oxygen plasma etching on lightweight plastic substrates are demonstrated. Furthermore, the fabricated nanobump-based metasurfaces have an excellent detection capability for carcinoembryonic antigen (CEA), suggesting that they are efficiently used in future flexible plasmonic biosensing systems. For further information, see Jiao et al.[22] and Langer and co-workers' significant contributions to the exploration of surface-enhanced Raman spectroscopy (SERS).[23]

Although plasmonic metasurfaces have desirable qualities such as substantial electric field enhancement, flexibility, and low weight for various sensing techniques, the inherent losses (Ohmic loss) of the constituent metals usually narrow down their large-scale commercialization. More specifically, the use of plasmonic nanostructures as one of the critical solutions of

surface-enhanced IR absorption spectroscopy (SEIRAS) demonstrates significant absorption enhancement in the mid-IR molecular fingerprint spectra.[24–26] However, plasmonic enhancement suffers from effective damping in noble metals and isolated narrow band enhancement, making broadband fingerprint detection difficult.[27–29]

The high field enhancement factor in case of plasmonic nanostructure is accomplished at the expense of substantial optical losses owing to metal absorption, which severely restricts its wide applicability.[30] Caldarola et al.[31] show a strategy that overcomes these restrictions by realizing a unique nanophotonic platform based on dielectric nanostructures to construct effective nanoantennas with ultra-low light-to-heat conversion. Finally, they found that dimmer-like silicon-based single nanoantennas exhibit strong surface-enhanced fluorescence and SERS while causing low-temperature increases in their hot spots and surrounding environment. Therefore, the use of dielectrics with low optical loss and a high refractive index (HRI) to replace the constituent materials (metals) of metasurfaces is a new way to get around these constraints. Because of their attractive optical properties, dielectric metasurfaces open a new horizon for nanophotonic sensing. Note that also do not perturb the target's response due to unwanted local heating. The utilization of dielectric metasurfaces in biomolecular barcoding has resulted in an excellent method for broadband fingerprint recognition. However, it requires a succession of sophisticated metasurfaces requiring specific nanofabrication and still lacks dynamic tunability on a fixed sensor structure. For example, various studies on dynamically tunable detectors to capture broadband THz absorption features have been conducted. Still, the detection enhancement is minimal, and the sensing configurations require temperature, bias voltage, or static magnetic field control, which is complicated by additional noise in practice. As a result, a flexible THz detection approach with significant broadband signal augmentation is still in high demand for biomolecular fingerprint sensing.

Our group recently designed a dielectric metagrating with polarization and angle modulation of an incident THz wave to advance molecular fingerprint detection.[32] The system is regarded as one of the first of its kind, as it dramatically reduces the intrinsic optical absorption that would otherwise interfere with sensing performance. The enhanced broadband detection of molecular fingerprint for identifying the trace-amount analyte of just 1 µm thick is reflected by the combined multiplexed signals obtained by dynamic angle scanning. Furthermore, we proposed another critical method based on a basic layered structure made of two un-patterned layers for excellent THz absorption in an ultra-thin material layer to get a closer look at the phenomenon of THz detection.[33] A comprehensive analysis based on coupled-mode theory demonstrates the physical prerequisites for perfect THz absorption. In addition, the impact of incidence angle, frequency, and dielectric thickness is extensively examined. The ideal absorption is attributed to the excitation of evanescent waves at the interface between the air and the layered structure. More efforts should be done for optimizing the light–matter interaction, in metasurfaces, for instance by polarization and angle tuning, in order to have higher sensing performance for more required analytes.[34–36]

We present a detailed overview of the current state-of-the-art for this rapidly emerging research topic, as well as a forecast for prospective future directions, in this publication. More intriguingly, the manuscript is structured, to begin with, a thorough introduction to metamaterials and metasurfaces, including the phenomena involved and their significance for optical biomolecular sensing. The quality factor and the numerous aspects that influence it are discussed in the following section. The dominant types of metasurfaces with the related phenomenon are next discussed. Furthermore, in the applications section, we comprehensively demonstrate the most common techniques for label-free sensing. Finally, we review the current challenges as well as the emerging trends.

2. Factors Which Influence the Q-factor (EM coupling)

The Q-factor is known as the ratio of the resonance wavelength to bandwidth. According to reports, the experimental Q-factor does not match with the theoretically predicted Q-factor, ascribed to poor spatial coherence of light beams,[37,38] fabrication imperfections,[39,40] tiny array sizes,[39–41] and the addition of an adhesive layer.[42] Therefore, comprehensive analyses on the factors that have the strongest influence on the measured quality-factor (Q) of an SLR (surface lattice resonance)-based metasurface is needed. Thus, the impact of nanostructure shape, spatial coherence, and array size of the probing source of light on reaching ultra-high Q-factor was thoroughly examined. Then, utilizing efficiently the findings of this section, we selected a plasmonic metasurface promising for the achievement of the extremely-high-Q SLRs.

2.1. Polarizability in Meta-Atoms or Meta Units

Individual metasurface structures are engineered in order to produce the most effective response during SLR. The polarizability of a Lorentzian dipole can be used to calculate the optical response of a nanostructure, as demonstrated by Equation (1)

$$\alpha(\omega) = \frac{A_0}{\omega - \omega_0 + i\gamma} \tag{1}$$

where A_0 is the oscillator strength, $\omega_0 = 2\pi c/\lambda_{LSPR}$ is the nanoparticle (NP) characteristic resonance frequency, while, γ represents the damping constant. The values of these magnitudes affected the geometry particle.[43] The LSA can be used to introduce the particles' lattice contribution to polarizability.[44,45]

$$\alpha^*(\omega) = \frac{\alpha(\omega)}{1 - \varepsilon_0 \alpha(\omega) S(\omega)} \tag{2}$$

where $S(\omega)$ is the lattice sum and $\alpha^*(\omega)$ shows the effective polarizability of the whole metasurface, which is solely determined by the lattice configuration. At $\omega_{SLR} = (2\pi c/\lambda_{SLR})$, an SLR achieved. Here $S(\omega)$ presents a pole. The individual responses of all of the nanostructures collectively contribute to this spectral location.[45]

In the case of metasurfaces with simple unit cells, the optical response of the metasurface as a function of the geometry of its nanostructures, including the behavior of its numerous resonances, may be calculated by using Equation (2). As a result, the change of the nanostructure geometry affects the individual wavelength of resonance λ_{SPR}, the strength of oscillator A_0, and the damping constant (γ). According to the well-recognized relationship between the geometry of NP and polarizability, the value of A_0 ranges up to 20% decrease in NP volume.[2,46,47] Accordingly, for each value of A_0 light can be coupled optimally to the lattice resonance at λ_{SLR}, leading to the maximum Q-factor. In other words, the best conditions are obtained when there is a perfect balance between the increasing α and P_y, which leads to enhancing the coupling strength and maintains a broad-spectrum gap between λ_{LSPR} and λ_{SLR} (i.e., limiting the loss known as Ohmic losses, caused by metallic NPs, occur).

2.2. Array Size and Fabrication Scheme

The array size is a key parameter that influences the metasurface's overall Q-factor, because the lattice disturbances near the array's edge break coherence, resulting in substantial scattering of light into free space and broadening of the resonance peak. Yang et al.[48] postulated that as the array size increases, the Q-factor improves, and eventually converges at 10 000-unit cells, which corresponds to an array size of 80 μm × 85 μm.

More intriguingly, bigger array sizes have been linked to improved device performance.[41,49,50] This dependency makes sense because, since high-Q operation requires low absorption loss, the device must operate far away from the LSPR. The relatively small scattering of cross-sections leads to suitably long operating wavelengths, resulting in relatively weak scattering for each antenna. As a result of the distance from the LSPR, a big number of scatters are required to build up a resonance. In an SLR, the standing wave mode is made up of surface waves with counter-propagation. Hence, array with larger size allows a longer length of propagation in the cavity that accommodates these modes.

Saad et al.[51] developed and analyzed a series of the fabricated devices with enhancing array size to investigate the impact of Q-factor on the nanostructures numbers. The transmission spectrum along with their semi-analytical predictions is shown in **Figure 1**a. As the array size enhances, the appeared Q-factors increase monotonously (Figure 1b). The SLR is negligible in the smallest array (300 × 300 μm²). Due to the sluggish writing-speed of the electron-beam lithography technology required for fabrication,[42,52] this tendency may show the comparatively lower Q-factor values presented in the previously reported studies,[39–41,53] where the size of arrays was typically smaller than that of 250 × 250 μm².

2.3. Spatial Coherence (Light Excitation, Incident Angle, Source)

In order to obtain an accurate measurement of the Q-factor, it is necessary to evaluate all features of the characterization system. The probing beam's spatial coherence is also an important parameter for achieving a clear measurement of the
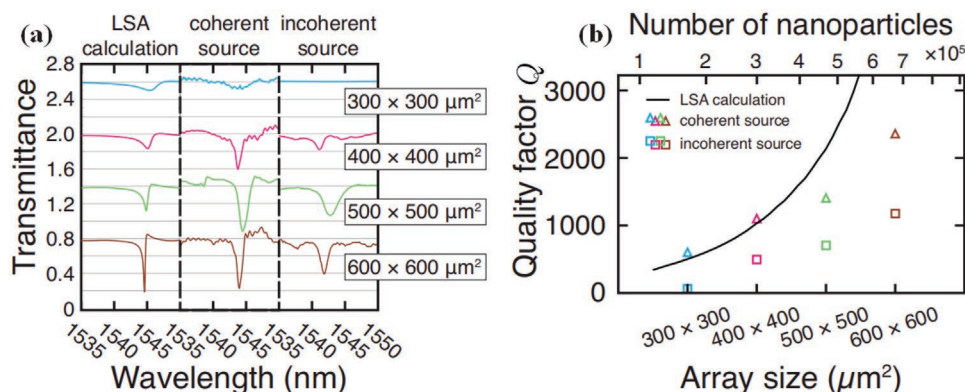
ADVANCED
SCIENCE NEWS
www.advancedsciencenews.com

ADVANCED
OPTICAL
MATERIALS
www.advopticalmat.de

Figure 1. a) Transmission spectra for the arrays of identical metasurface of various sizes (from top to bottom: 300 × 300, to 400 × 400, to 500 × 500, and 600 × 600 μm²). b) Q-factor calculated from Lorentzian fitting to the results of computations and measurements.[51] Reproduced with permission.[51] Copyright 2021, Springer Nature.

transmission drop which indicates a resonance. In comparison to a spatially incoherent source which can be employed, a beam of spatially coherent light, such as the laser that excites every region of the fabricated metasurface in phase, resulting in a resonance characteristic that is both narrower and deeper. Furthermore, when incoherent sources are used, the lattice's higher-order modes are highly sensitive to angular variance during observation, resulting in bigger peaks.[38]

Figure 1 demonstrates a comparison of the performance/efficiency of the metasurface when it is irradiated with various sources of light. The sources of excitation include a broadband supper-continuum laser which is a well-collimated source of coherent light and a lamp of tungsten-halogen. The Q-factor increases with the light source coherence. A thermal light source decreases the value of Q-factor by 2–5 times, compared to a laser. Furthermore, the reduced SLRs' extinction ratio suggests a decrease in resonance coupling strength.

The Q-factors calculated from these data are summarized in Figure 1b, where they are also compared with numerical calculations results. According to LSA calculations, Q-factor enhances as the array size increases. This conclusion is valid for both small and big devices. Even with a source of incoherent light, the biggest array provides an extremely high value of Q-factor, that is, Q ≈ 1000. The achievement of the high Q-factor with a source of incoherent light confirms that a metasurface can be also designed by taking into account other criteria, namely the importance of array size and nanostructure geometry.

Similar to the quality factor (Q), the figure of merit (FOM), defined as the ratio of sensitivity (S) to full width at half maximum (FWHM) of the reflectance dip, is a comprehensive metric to evaluate the performance of an appropriate metasurface based biosensor. Improving sensitivity, according to the concept of FOM, is an immediate way to improve FOM. Many studies have been carried out in recent years to increase sensitivity. Lahav et al.,[54] for example, improved sensitivity by using a guided-wave surface plasmon resonance (SPR) structure made by evaporating a 10 nm Si layer on top of a metal substrate. Both Shukla et al.[55] and Bao et al.[56] showed that adding a ZnO thin film to an SPR sensor enhanced its sensitivity. Furthermore, Benkabou et al.[57] improved the sensitivity of the SPR sensor by using a dielectric multilayer construction.

3. Metasurfaces for Optical Biosensing

It was Veselago who foresaw in 1968 the advancement of synthetic materials by manipulating their characteristics, such as permittivity and permeability.[58] Pendry et al.[59] and Smith et al.[60] were the first who discovered this, providing proofs to Veselago's theory and revolutionizing our understanding on the EM response of certain light–matter interaction problems, such as negative refractive index (RI) materials, electromagnetically induced transparency (EIT), optical clocking, etc. Metamaterials are a type of artificial composites made up of subwavelength metal/dielectric micro/nanostructures that are resonantly coupled to the electric/magnetic components of incident EM fields. More intriguingly, the prepared artificial micro/nano-structures demonstrate several unique properties for manipulating light, including a variety of stimulating novel optical effects and functions that natural materials do not.[61,62]

During the last 15 years, this class of the micro/nano-structured artificial composites has received a sharp attention and generated ground-breaking EM and photonic phenomena. However, practical applications of metamaterials have been hampered by high loss and bad dispersion attributed with resonant response and the use of metallic structures, as well as the difficulty in fabricating micro and nanoscale 3D structures.

Fabrication of planar metamaterials with the subwavelength thickness or metasurfaces was a difficult aspect and often a limitation in the past,[63–66] but it has significantly improved and can now be prepared using lithography and nano-printing mechanisms, where the ultrathin thickness with the direction of wave propagation significantly suppresses the unwanted loss. Metasurfaces allow spatially changing optical responses (e.g., phase, scattering amplitude, and polarization), the molding of optical wavefronts into custom shapes, and the incorporation of functional materials to achieve active control and a great enhancement of nonlinear response.

Furthermore, metasurfaces with reduced size are fabricated easily, compared to conventional optical elements. More interestingly, they are prepared from an optical element decorated on the surface with subwavelength size. The produced wavefront of light shows a spatial profile of the optical phase. This led to the development of ultrathin optical elements, which are

superior to the corresponding bulk materials.[53,67] Additionally, these novel devices demonstrate a large range of EM spectrum from visible to THz frequencies.[68] These metasurfaces-based flat devices are a new type of miniature, flat, and lightweight elements. Outstanding progress has been reported in the development of metasurfaces for molecular optical sensing.[69–73]

3.1. Types of Metasurfaces

The optical metasurfaces are categorized into metal and dielectric metasurfaces. The metal metasurfaces rely on surface plasma oscillations of subwavelength metal particles. On the other hand, low energy dissipation, due to Ohmic loss induced by metal structures, is significantly difficult, especially for devices operating in transmit modes. Dielectric metasurfaces that are based on the Faraday–Tyndall scattering of high-index (HI) dielectric light scattering particles demonstrate reduced loss but they display similar functionality.

As a result of the development of suitable designing of relevant unit structure parameters, such as size, geometry, and direction, several metasurface functions can be obtained, allowing a wide variety of applications. Due to the unique EM characteristics, metasurfaces with various design have the ability of manipulating the phase, amplitude, and polarization of EM wave. Thus, metasurfaces are promising for wavefront modulation, such as beam focusing, beam steering, vector beams generating, and holographic imaging.[74,75] However, the focus of this study is on the design and physics of metasurfaces for biomolecular sensing applications. This section focuses on the design of various characteristics, such as anomalous reflection, refraction, and the functioning principle of the two types of metasurfaces.

3.2. Plasmonic Metasurfaces

Metamaterials is a term used for a wide family of artificially designed materials with outstanding and unique features that are superior to naturally occurred materials. Their distinct properties are attributable not just to the chemical composition, but also to the structure, that is, spatially designed geometry.[76–78] Nowadays, it is evident that the initial development of the metamaterial-based devices (metasurfaces) will most likely be inspired by their 2D counterpart metasurfaces.

The plasmonic metamaterials are made up of meta-atoms designed from metallic nanostructures, whose optical response is governed by the plasmon resonances that they support. Many applications in photonics need metallic nanostructures, including biosensing, spectroscopy, nanolaser, metasurface technologies, nonlinear optical processes, and all-optical switching.[53,79–83] These plasmonic elements manifest numerous desirable properties, including the ability to successfully confine the light into sub-wavelength scale and important local-field improvements.[46,53] In addition, metals have intrinsic nonlinear optical constants that are several orders of magnitude higher than dielectrics.[84]

According to the physics of optical resonance in metallic/plasmonic metasurfaces, each nanostructure display localized plasmon resonances (LSPRs) when they are structured at a sub-wavelength scale,[53,83,85] at the metal-dielectric interface, EM fields couple to a conductor's free-electron plasma.[46,86,87] More interestingly, depending on its geometrical shape, an individual NP can be polarized by an incident light beam, which acts as a dissipating dipole antenna and traps light for a brief period.[88] The resonant dipoles in a metasurface can be assessed easily by a beam propagating in empty space and needs only a sub-wavelength propagation region, compared to other photonic resonant devices, such as micro-ring resonators, photonic crystals, or whispering gallery mode resonators.[51,89–91] As a result, a plasmonic metasurface resonator can provide a variety of special optical effects, such as highly localized field enhancements,[53] phase-matching-free nonlinear optical effects,[92,93] specially localized optical response,[82] and multi-mode operation.[94]

However, one of the most widely reported limitations of LSPR-based metasurfaces is the lower value quality factor, that is, $Q < 10$, which is attributed to the inherent Ohmic losses found in the metals at the range of optical frequencies.[46,71,95,96] Because the quality-factor (Q-value) is directly linked to both electric field enhancement as well as the light–matter interaction time, it is usually highly desired to increase this value.[89] The optical response of the paired plasmonic nanoresonators has piqued the subject of research interest.[97] SLRs are collective resonances supported by plasmonic metasurfaces of massively periodically-organized nanostructures.[39,40,52,98] The individual surface plasmon responses from many individual nanostructures are combined to provide a collective response that is linked to the periodic array's in-plane diffraction orders.[39,52]

An overview of the recent progress in the development of high Q-factor plasmonic metasurfaces is presented in Figure 2. Dayal et al.[99] demonstrated a multi-resonant plasmonic metasurface with a line-shape and line-width of the super-radiant and sub-radiant modes that can be adjusted to fit particular vibrational modes using a giant field augmentation. **Figure 2**a shows a schematic perspective of the suggested metasurface design as well as scanning electron microscopy (SEM) images. It is made up of two annular apertures that are concentric. A rectangular aperture overlaps the outermost annular aperture. The outermost radius of the nth annular aperture is indicated by $R_{n,o}$ in this diagram. The aperture width was kept constant at 100 nm for all of the apertures.

The superposition of the super-radiant mode with the sub-radiant mode results in high Q-Fano resonances in the reflection spectrum of the fabricated metasurfaces. The line-shape, line-width, and spectral location of the super-radiant modes and Fano resonant modes may all be tuned efficiently. In addition, a new way was proposed for controlling the asymmetry parameters of Fano resonances. The fabricated metasurface exhibited an adjustable multispectral response. This suggests it is an excellent candidate for studying light–matter interactions, especially surface-enhanced infrared absorption (SEIRA), which allows simultaneous monitoring of numerous different molecular vibrational modes. This was validated by multi-band surface-enhanced IR spectroscopy (MSEIRS) performed for polymethyl methacrylate (PMMA). The metasurface carefully engineered the plasmonic resonances that can be easily adjusted to fit the various vibrational modes of PMMA in the range of the mid-IR region.
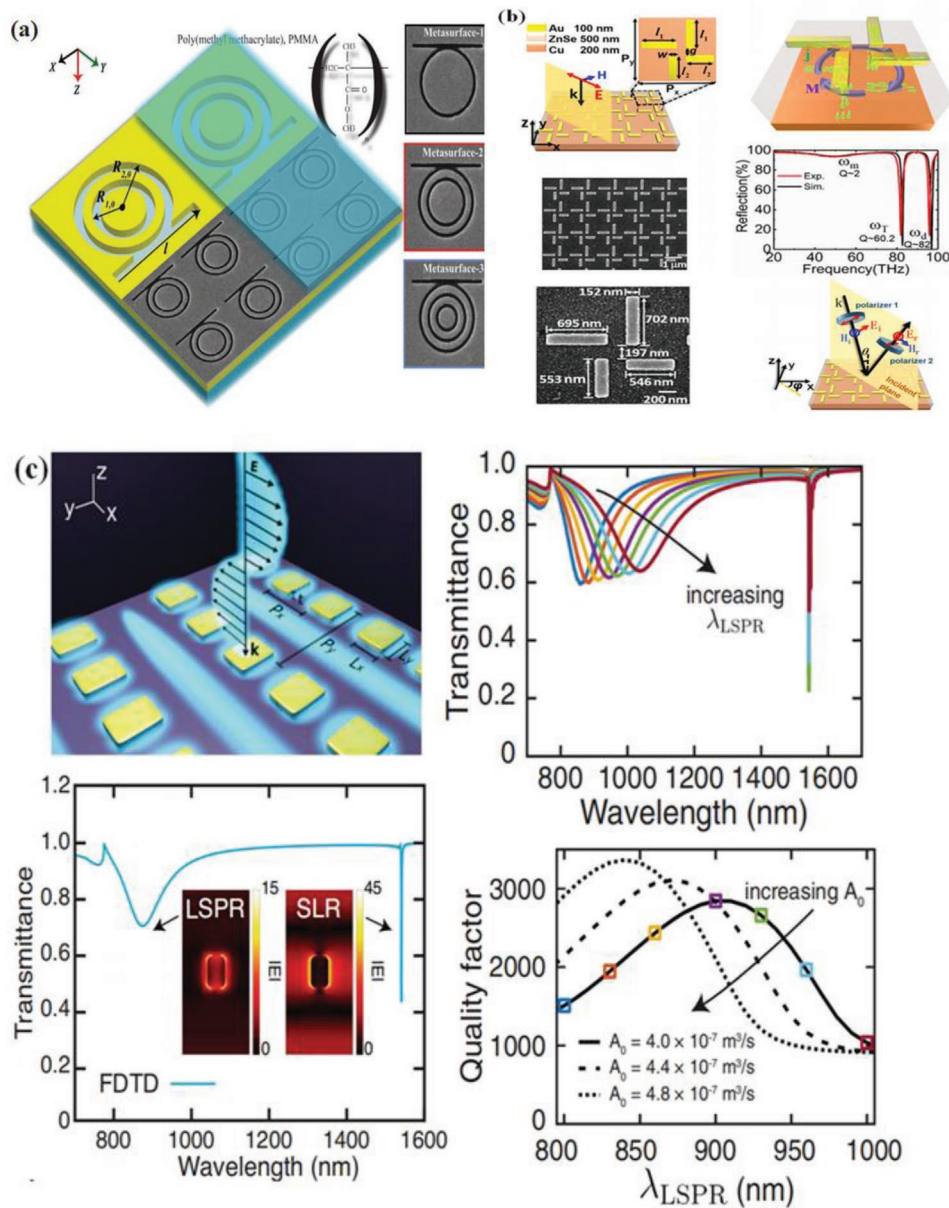
**ADVANCED
SCIENCE NEWS**

www.advancedsciencenews.com

**ADVANCED
OPTICAL
MATERIALS**

www.advopticalmat.de

Figure 2. a) Metasurface, depicted schematically as a series of concentric circular and rectangular openings, along with SEM images.[99] b) Schematic illustration of the design along with SEM images, measured and computed reflection spectra, and illustration of the measurements of the cross-polarized and co-polarized reflection spectra.[100] c) Schematic representation of the design with various features, like transmission spectra calculated by FDTD, transmission spectra as function of λ_{LSPR}, and the SLR's Q-factor as a function of λ_{LSPR}.[51] (a) Reproduced with permission.[99] Copyright 2016, Wiley-VCH. (b) Reproduced with permission.[100] Copyright 2020, AIP. (c) Reproduced with permission.[51] Copyright 2021, Springer Nature.

The multipole moments coupling in the structure of subwavelength reveals new possibilities for creating metamaterial features. Liu et al.[100] reported on a hybridized resonance with a good Q-factor from the magnetic dipoles' alignment in the developed metasurface of plasmonics made of asymmetrically constructed metal bars the planar of metal–insulator–metal (MIM) structure. By constructing four metal bars of two different lengths in a cross-configuration in a planar MIM structure, a strong hybridized resonance mode at 82.6 THz with a Q-factor of 60.2 was achieved experimentally.

In RI sensing, a hybridized metamaterials mode with a high Q-factor demonstrates polarization-selective excitation, a high-figure-of-merit (FOM), and a conversion of cross-polarization. The structure of the prepared metasurface as well as an SEM image is shown in Figure 2b (left). The metasurface is built of the ground copper film with a thick layer of ZnSe dielectric of about 500 nm and an array of four gold bars that are asymmetrically patterned. Coupled current loops resulted from the combined excited surface currents in the metal bars and their image currents in the ground metal, forming a hybridized

resonant mode with a ring of head-to-tail (Figure 2b, right-top) connected magnetic field for an incident electric (E) field polarized along the unit cell's diagonal direction. The recorded and computed reflection spectra of the sample for an incident polarization along the diagonal direction of unit-cell are shown in Figure 2b (right-middle). Two high and steep absorption peaks were recorded at 82.6 and 95.6 THz, as well as a shallow dip at 53 THz. The experimentally obtained resonance characteristics are in excellent agreement with the theoretically achieved spectrum.

The four aligned current loops that make up the hybridized resonance mode mentioned above are sensitive to the incident polarization. The influence of metasurface polarization was thoroughly investigated. As shown in Figure 2b (right bottom), a second polarizer was placed in front of the detector to allow recording of both cross-polarized and co-polarized reflectance, R_{cr} and R_{co}, respectively. According to the findings, the polarization angle has negligible effect on the mode at $\omega_m = 53$ THz. Meanwhile, the mix mode at $\omega_d = 95.6$ THz weakly depends on polarization angle, with reflectance fluctuations of less than 15%. The hybridized resonance mode at $\omega_T = 82.6$ THz, is more polarization sensitive. Maximum excitation was obtained at the three polarization angles, that is, $\varphi = 45$, 15, and 75°.

Accordingly, a reasonably immense Q resonance occurs at an optical wavelength of $\lambda_{SLR} \approx nP$, which is nearly equal to the multiplication of the background medium RI (n) and the lattice period (P).[52,101] To appropriately engineer the size and the period of the lattice for the individual nanostructures, theoretical analysis should be conducted. A recent development indicated a high projected Q-factor (about 10^3).[40,101,102] This allows to combine the advantages of metals with the long period interaction given by high quality-factors (Q). However, an SLR-based metasurface with the highest Q-factor at about 430 was also obtained experimentally.[103] As discussed above, the small array size,[39–41] the low spatial coherence of the light beam,[37,38] the insertion of an adhesive layer,[42] and the fabrication flaws[39,40] all contribute to the discrepancy between theoretical and experimental results.

The above mismatch stimulates the interest to thoroughly analyze the numerous parameters that influence the Q-factor of SLR-based metasurfaces. The geometry and the size of nanostructure arrays as well as the probing light source's spatial coherence are the most important factors that influence the Q-factor. Saad et al.[51] used the results of such analysis to develop a plasmonic metasurface that is suitable for the supporting of exceedingly-high-Q SLRs. As shown in Figure 2c, the suggested metasurface is made up of a rectangular array of the rectangular gold nanostructures implanted in silica glass with an RI of $n \approx 1.45$. The characteristics lattice constant was chosen in such a way that the SLR wavelength was fixed in the telecommunication window by setting $P_y = 10$ nm. The square lattice was lowered to $P_x = 500$ nm, enhancing the NP density and, as a result, the resonance's extinction ratio, as well. Because the homogeneity of the surroundings influences the Q-factor, the over-cladding is appropriately adjusted to the materials of substrate which provide a symmetric cladding index.[44,52,104] Figure 2c (below left) displays the numerical projections for the created metasurface's x-polarized beam, which demonstrate that the presented metasurface is expected to sustain an LSPR

at $\lambda_{LSPR} = 830$ nm, while an SLR of the first kind at around $\lambda_{SLR} = 1550$ nm is maintained. Figure 2c (right-top) shows the experimentally recorded transmission spectrum, which is a good match to the predicted calculated spectrum. The FWHM of the line width is just $\Delta\lambda = 0.66$ nm, which corresponds to a Q-factor of 2340. This value is higher by an order of magnitude than the previous record for plasmonic metasurfaces, and is among the highest values ever documented for a metasurface.

The computed transmission of the metasurface is presented as a function of nanostructure resonance wavelength λ_{LSPR} and λ_{LSR} to demonstrate the dependence in this platform explicitly (Figure 2c, right-top). The position of resonance is slightly tuned from the dip position in the case of LSPR, due to the long-wavelength correction. On the other hand, the LSR wavelength does not shift noticeably from its current point around $\lambda_{SLR} = 1542$ nm. However, the resonance extinction ratio ΔT and the line-width $\Delta\lambda$ are altered substantially. The measured quality-factors (Q) for these SLRs as well as other values of A_0 are plotted in Figure 1b. According to the well-established relation between the NP polarizability and geometry, the range of A_0 corresponds to a 20% alteration in NPs' volume.[46,105] For each value of A_0, there is an λ_{LSPR} where the light is optimally coupled to the lattice resonance at λ_{SLR}, leading to the maximum Q-factor.

3.3. Dielectric Metasurfaces

Metasurfaces, which are made up of metallic or dielectric metacells, attract remarkable attention in optical applications, like imaging[106–110] and meta-lenses,[111–117] because of their ability to adjust the phase, polarization, anisotropy, chirality, and to amplitude of light arbitrarily.[64,82,118–120] Because of the intrinsic Ohmic losses of metals, plasmonic metasurfaces can be perfect absorbers.[121–127]

Because of their low losses and magnetic responsiveness, particles composed of HRI dielectric materials have been offered as a substitute for metals. The outstanding directionality of electric and magnetic resonances is due to their coherent effects, which make them appealing in applications where enhancing light–matter interaction and regulating radiation direction is critical. When utilized as unit cells in more complicated systems, such as metasurfaces, these NPs become critical in constructing innovative optical devices. These nano-antennas are exciting candidates for surface-enhanced spectroscopies (SESs), non-linear phenomena, and sensing because of their low losses, robust confinement of EM energy, and high scattering efficiency. This section describes the current advancements in the fast-emerging area of dielectric nanophotonics.

Dielectric resonators/dielectric metasurfaces can efficiently support strong electric and magnetic resonances at optical frequencies.[128–135] The Mie theory may be used to describe the resonances of a spherical or spheroidal particle in particular. Kerker et al.[136] discovered that it is feasible to control the direction of light scattered by point-like magnetodielectric particles (Kerker conditions) by suppressing either the backward or forward scattered light. This breakthrough sparked research on high-refractive-index subwavelength dielectric particles, such as silicon or germanium. Unlike metals, these particles exhibit
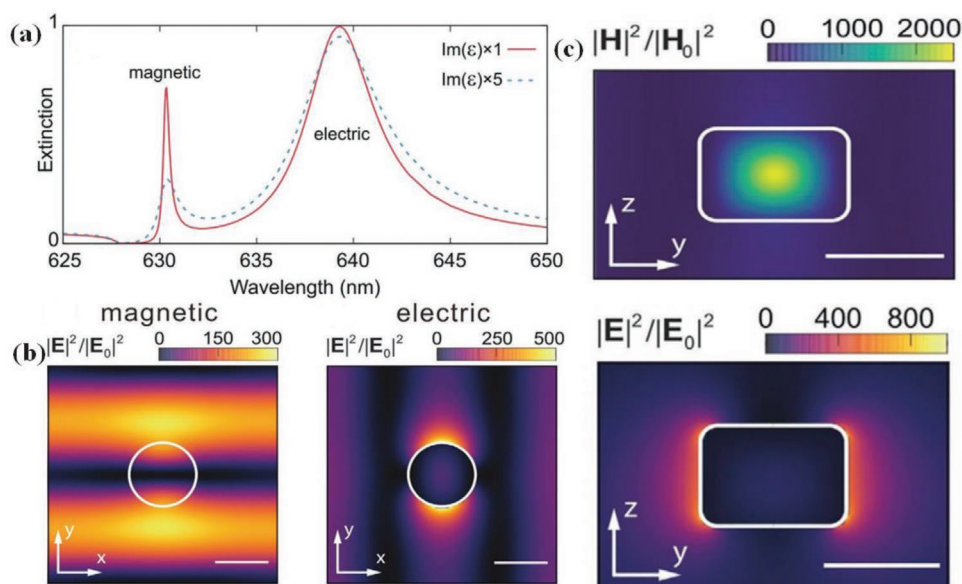
**ADVANCED
SCIENCE NEWS**

www.advancedsciencenews.com

**ADVANCED
OPTICAL
MATERIALS**

www.advopticalmat.de

Figure 3. a) Extinction spectra (simulated) for the Si NP array with a period of 430 nm and diameter of the particle $d = 126$ nm implanted in a homogeneous medium with RI $n = 1.46$ at $\theta_{in} = 0°$ at around the Rayleigh anomaly. The overall field intensity in a unit cell is distributed spatially as follows: b) Magnetic M-SLR field intensity ($\lambda = 630.3$ nm) with xy and yz planes crossing the NP at its center. c) The electric field intensity of M-SLR. The white curves represent the boundaries of NPs.[149] Reproduced with permission.[149] Copyright 2020, Wiley-VCH.

both electric and magnetic mode resonances, suggesting that they might be used as building blocks for new photonic platforms to efficiently regulate light scattering direction.[137–140] Exploring HRI dielectric topologies and finding innovative, efficient techniques to regulate the directionality of light propagation in a broader sense, including improving scattering in the forward and backward directions and adding light steering or switching, was a major focus.[141–143] For example, isolated spheroids,[133,144] dimmers, aggregates,[145,146] or core-shell particles,[147,148] and materials like Si, GaP, Ge, and others, have been all investigated.

As a result, the extinction spectrum shows the peaks of electrical and magnetic Mie-SLR (M-SLR), as seen in **Figure 3**a.[149] The first peak at ≈630.3 nm is assigned to magnetic M-SLR, whereas the second one at ≈639.3 nm is attributed to electric M-SLR. The simulation results are shown with the solid line in the extinction spectrum, whereas the experimental data are shown by the dashed line. There is perfect matching between the two plots. Figure 3b, (left bottom) shows the explicit signatures of M-SLRs in the intensities of the electric field at the resonant wavelengths in the plane of unit-cell. Unlike localized resonances, where the variation in field intensity is confined to the NPs, an intense pattern spanning across the unit cell is observed. The intensity of magnetic field of M-SLR in the NP's yz-cross-section is markedly enhanced inside the volume of NP that is typical for magnetic dipole resonances (Figure 3c, top). On the other hand, electric M-SLR has stronger electric field strength near the NP's vertical edges, which is an indication of electric dipole resonances (Figure 3c, bottom). The relationship between a dielectric NP's resonance wavelength and its dimension is $g(\lambda/n) = 2\pi r$, where g is a positive integer, λ is the resonance wavelength, and r is the radius.[150,151] The resonance wavelengths of the dielectric metasurfaces may be easily tuned

from visible[152,153] to the IR spectral region,[154,155] according to various sensing mechanisms which involve efficient altering of the size of the meta-atoms and materials. These outstanding properties have motivated the development of a variety of sensing metasurfaces.

Various aspects, related to resonance bandwidth, operating wavelength, resonance quality, and field enhancement, must be carefully considered in the design of dielectric metasurfaces optical sensing in order to achieve the desired functions of metasurfaces with high precision. The Q-factor is a key characteristic of dielectric metasurfaces for various phenomena, such as SES, similar to plasmonic metasurface analogs. A narrower bandwidth is associated with a larger Q-factor, which is a significant limitation for numerous techniques such as SEIRA and vibrational circular dichroism (CD) spectroscopy.[156] A narrower resonance, which implies a smaller spectral bandwidth, may be unable to cover sufficiently the molecule bands of absorption for a specific chemical detection. Accordingly, it is critical to be aware of these limitations and to think about creating device designs that can benefit from the high-Q value, while they still display broad-spectrum coverage, as in the cases outlined in this section.

Toroidal mode is a type of EM excitation out of traditional electric and magnetic multipole models. Because of the weakly radiating behavior and the capacity to contain EM radiation, it is currently a hot topic in modern research on nanophotonics and metamaterials. However, despite the intensive research on the toroidal moments and their various applications, toroidal resonance with high-quality factor (Q) has only been achieved experimentally in limited wavelengths and geometries. Jeong et al.[157] used silicon (Si) as the HI dielectric to obtain experimentally a relatively high Q-factor as 728 at 1505 nm wavelength, which is one of the highest Q-factor values reported
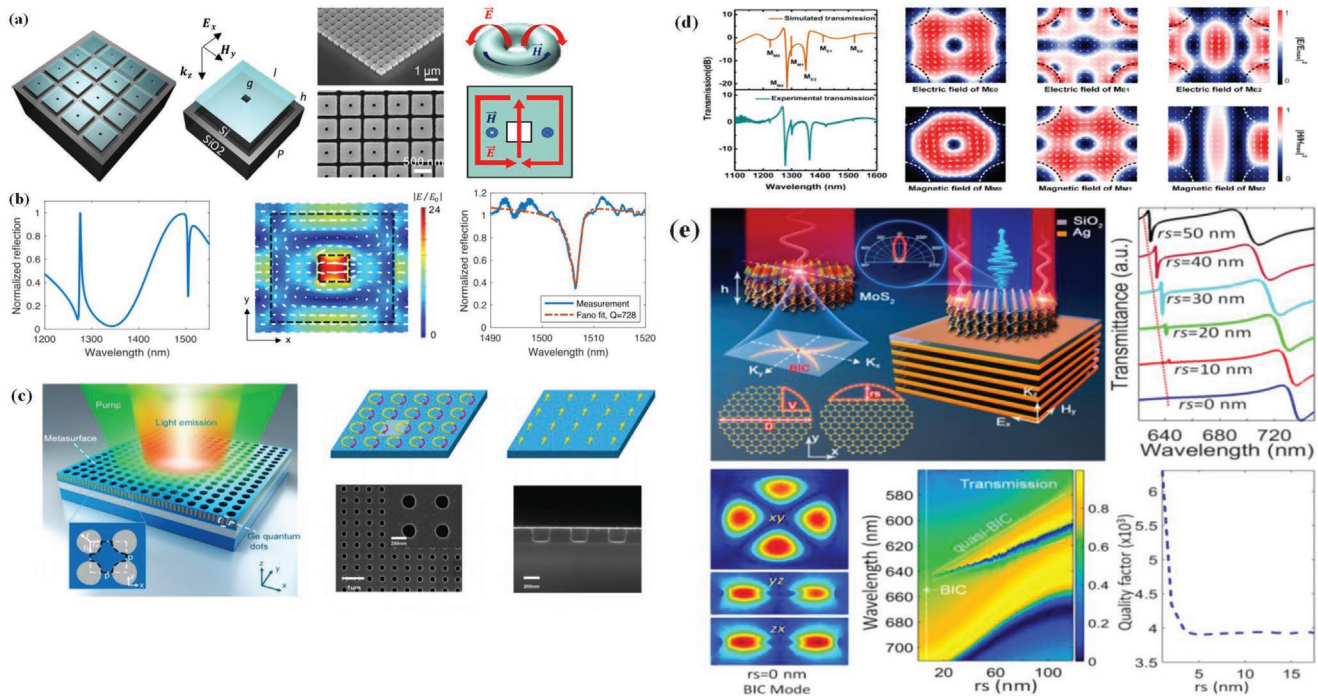
Figure 4. A dielectric hollow cuboids array used to generate a toroidal resonance with a high-quality factor (Q). a) The schematic illustration of the image of silicon (Si) cuboid metasurface with top-angle SEM image of array, the profile of the solenoid electric fields (red arrows) creating a toroidal magnetic field in a torus (blue arrow), and b) the sample's simulated reflection spectrum. The steep dip at 1505 nm is caused by interference between the toroidal dipole resonance and the magnetic quadrupole resonance. Profile of the electric field at 1505 nm in the center of the resonator ($z = h/2$). Fano fitting result of the resonance at 1505 nm, which produces a Q-factor of 728 and a linewidth of 2.1 nm, yields a distinct signature of the toroidal dipole mode with an electric field increase of up to 24.[157] c) Fano resonance configuration with schematic illustration of Fano metasurfaces and SEM images. d) Experimental and computed spectra of relative transmission of the metasurface using the method of FDTD, profiles of electric and magnetic modes, and field vector distributions for electric and magnetic modes.[158] e) Schematic representation of a MoS₂ nanodisk with directed emission, showing the profile of transmission spectra, transmission spectra with respect to rs values, the magnetic field distribution around BIC at rs = 0 nm, and quality-factor (Q) at various rs values, and other related features.[162] Reproduced with permission.[157,158,162] Copyright 2017, 2020, and 2021, American Chemical Society.

for a dielectric metasurface in the near-IR. More crucially, the resonator design provides exceptionally efficient toroidal resonance coupling to the environment, attributed to the built-in geometry. With a satiable line width of 2.01 nm and a sensitivity of 161 nm per RI unit, an index change of less than 0.02 was reached for the designed metasurface.

A subset of the samples is graphically presented in **Figure 4**a, coupled with scanning electron microscopy images. A dense array of dielectric hollow cuboid resonators is used. Two arrays of these mentioned resonators, which have resonances in the visible (titanium oxide) or near-IR (silicon), were investigated. It is interesting that the solenoidal electric field travels in-plane along the rectangular channel, while the toroidal magnetic field circulates out-of-plane around the center void due to the geometry of the hollow cuboid structure.

Numerical simulation was conducted using commercially available FDTD solver software (Lumerical). The behavior of an endless array was approximated by putting periodic boundary constraints on the array's unit cell. By gradually enhancing the resolution of mesh, the convergence of the solution was tested. Figure 4b (left) shows two resonances with Fano-type line morphologies at around 1280 and 1550 nm in a simulated reflection spectrum. It was concluded that the overlapping of electric and toroidal quadrupoles is responsible for the reso-

nance at 1280 nm. On the other hand, the strong Q resonance at around 1505 nm was attributed to the resonance of toroidal dipole. The electric field of solenoid for the resonance at 1505 nm closely follows (schematically illustrated in Figure 4a), which clearly suggests the presence of a strong toroidal dipole, as seen in Figure 4b (middle). Furthermore, the electric field was enhanced up to 24 times in the middle of the central hole, which is greater by a factor of e_{Si}/e_{air} than the field inside the dielectric. A linewidth of 2.1 nm and a Q-factor of 728 (Figure 4b right) is obtained by fitting a Fano-line shape to an appropriate narrow dip, which associates with the toroidal resonance that is indicative of a magnetic quadruple. This is a huge increase over earlier reported values of 200–600 in asymmetry-based dielectric resonator arrays, and it is one of the greatest Q-factors in dielectric metasurfaces.

Yuan et al.[158] proposed another approach for attaining an efficiently high Q-factor in the dielectric metasurfaces by constructing an asymmetric array of air hole on a silicon plate. A high-quality factor (Q) and noticeable Fano line shape were achieved by using the all-dielectric asymmetric metasurface structure. In the constructed all-dielectric metasurface, a three-order of magnitude boost of photoluminescence was observed, with a quality factor of 1011, which is a record-high value. The coherent Fano resonances, which are results of the destructive

**ADVANCED
SCIENCE NEWS**
www.advancedsciencenews.com

**ADVANCED
OPTICAL
MATERIALS**
www.advopticalmat.de

interferences of the antisymmetric displacement currents in the asymmetric all-dielectric metasurface, are responsible for the observed high photoluminescence emission enhancement.

Figure 4c schematically illustrates the suggested Fano metasurface, as well as SEM images and the origin of the high-Q value of the trapped mode. The structure is made up of an SOI slab with four layers of self-assembled Ge-QDs and a periodic lattice of asymmetric air holes implanted in it. When the emission of Ge-QDs is coupled with the asymmetric nanoresonators in the metasurface, a pair of anti-phased dipoles is excited in each unit cell. Due to structural asymmetry, the moments of the two neighboring dipoles are varying. In such a displacement current setup, most of the components of dipole radiation are negative due to destructive interference. Therefore, the scattered EM fields developed by the leftover dipole components are quite weak. As a result, the metasurface structure's radiation loss markedly decreases and the quality factor significantly increases.

To further study the properties of resonance mode, the experimentally recorded transmission spectrum is plotted in Figure 4d and it is compared with the results from finite difference time domain (FDTD) simulation performed under the normal incidence of an unpolarized plan wave. Six modes were observed in the wavelength range of 1100–1600 nm, termed M_E and M_M according to the field distribution. Furthermore, four sharp resonant peaks ($Q \approx 100\,000$), labeled as M_{E0}, M_{E1}, M_{M0}, and M_{M1}, associated with the modes coming from the relatively small difference of RI that is the result of weak asymmetry hole shape. The two wideband resonant peaks ($Q \approx 100$) resulted from the higher difference of RI, caused by the presence of holes in the unit cell. The various origin of each mode may be a result of their field vector distribution. The profile of the resonant peaks and their related field vector distribution are displayed on the right-hand side of Figure 4d.

Recently, a new and more efficient technique, based on the bound state in the continuum (BIC) for achieving high-Q metasurfaces, has attracted a lot of interest.[159–161] BIC has been widely researched in NPs with an infinite Q-factor, which is particularly fascinating. Muhammad et al.,[162] reported on Mie type resonance in a BIC-based molybdenum bisulfide (MoS_2) nanoresonator exposed in the air. A symmetry-protected BIC was also supported by an ultrathin nanodisk, and a quasi-BIC (q-BIC) was created by breaching the structure symmetry. Unlike previous reports on silicon-based devices, the tightly confined modes in the MoS_2-based nanodisk maintained an identical profile of magnetic field prior and after symmetry breaking. A hybrid arrangement with a resonator put on the top of stacked metal-dielectric layers that transforms BIC to q-BIC and exploits extremely directional light, produced strong directional emission in the BIC domain. Figure 4e shows a schematic representation of a nanodisk floating in the air, as well as a top view of semispherical rs, directional emission, transmission spectra, the characteristic magnetic field distribution around BIC at rs = 0, the transmission spectra in relation to rs values, as well as the Q-factor. The incorporation of symmetry breaking can cause a drop of the Q-factor for the small rs cutedges. At the cut-edge at rs >10 nm, the drop of Q-factor is minimal because the BIC is converted to a leaky resonance mode; additionally, there is no considerable rise in the number of radi-

ation channels, resulting in a small change in the Q-factor. The conversion of BIC can be tuned leading to q-BIC. Therefore, the resonance is displayed in the transmission spectrum with a specific spectral width and Q-factor. Consequently, the Q-factor can be efficiently tailored to the desired value, according to the demands of each application, by using the transformation approach of BIC to q-BIC in sub-wavelength structures.

4. Applications of Metasurfaces for Molecular Optical Sensing

Molecular optical sensors are used in a variety of applications, including security, environmental monitoring, bioanalytics, and diagnostics,[1,163–165] covering the range from visible to IR light, either dispersed or absorbed by the target. These sensors are non-invasive and provide high sensitivity since they work in the optical far-field regime.

In metasurfaces, there are four major approaches which can be involved in molecular optical sensing applications. Refractometric sensing, SES, surface-enhanced thermal emission (TE) spectroscopy (SETES), and chiral sensing are some of the techniques used. This section aims to shed light on each strategy.

4.1. Refractometric Sensing (Refractive Index Sensing, vs. Conventional Prism-Based SPR)

Nowadays, RI-based label-free optical sensing is the most successful and widely used technique because of the great performance, ease of use, and low cost. These sensors are used in a wide range of applications. They also display the advantages for reduced size and multiplex detection of many analytical targets at the same time. Metasurfaces with metallic[166] and dielectric nanostructures[167] alter scattering of light in the sub-wavelength regime, and, therefore, are very promising in a variety of applications.[168] The size/scale, and geometric shape of the metagrating structure, as well as the surrounding environment, is particularly sensitive to wavelength-dependent light scattering at metasurface building blocks.

The high sensitivity of the refractometric sensing of the compounds attached or adsorbed to the corresponding nanostructures is attributed to the substantial dependence of light scattering on the local environment surrounding nanostructures.[169] Various devices of the metasurface with dielectric and metallic materials have been intensively researched for the detection of air and water pollution, biomarkers, hazardous gas, and several other threaten-relevant and inspection-relevant species, with a sub-wavelength size/scale of the metasurface building units and an intensively high electrical field near the surface of metasurfaces.[170–173]

A conventional method for detecting spectrum variation in the light scattering induced by the presence of a little amount of target molecule is spectroscopy. However, spectrometers with high resolution and sensitivity are required for detecting very small amounts of a substance. A spectrometer with these features is costly, bulky, and requires a high level of skills. This frequently obstructs everyday molecular detection applications, such as monitoring of environmental quality, food safety,

**ADVANCED
SCIENCE NEWS**

www.advancedsciencenews.com

**ADVANCED
OPTICAL
MATERIALS**

www.advopticalmat.de

biomedical detection with point of care, and other applications that demand compactness, and ease of operation with consideration of cost-effectiveness.

Space-multiplexed imaging (SMI) based molecular identification detects particularly changing nanostructures.[173–175] Under narrow-band light illumination, appropriately developed with spatial alterations in the nanostructures, position-dependent transmittance or reflectance can be achieved because of the structure-dependent light scattering feature, resulting in a pattern. The presence of analyte molecules on the surface of metasurface modifies this pattern, which can be captured by a camera. This novel sensing approach has demonstrated an astonishing tremendous sensitivity using a considerably simplified equipment setup, which combines an advanced manufacturing of the metasurface nanostructure and high sensing performance. Min et al.[176] presented a centimeter (cm) scale plasmonic metasurface with regular but appropriately adjusted

holes and pillars for ultrasensitive, spectrometer-free, and label-free detection of a single-layer of the molecules adsorbed on a surface.

The suggested sensing technique is set up using continuously altering gradient of plasmonic metasurfaces to efficiently map the spectral information to particular locations, allowing SMI-based quantifiable molecular detection. More specifically, a narrow-band light source illuminates the detecting chip, and a commercial image sensor records the transmission pattern (**Figure 5**a). Two different sites, identified as positions A and B in the zoomed plot of transmission spectrum, are selected in order to explore the differences in intensity and wavelength of the resonance region. The red strip denotes the illuminating narrow-band light source. The resonance wavelength at position A is shorter than the illumination light source wavelength under n_1, whereas, the resonance wavelength at location B is longer than the illumination light source wavelength. As the
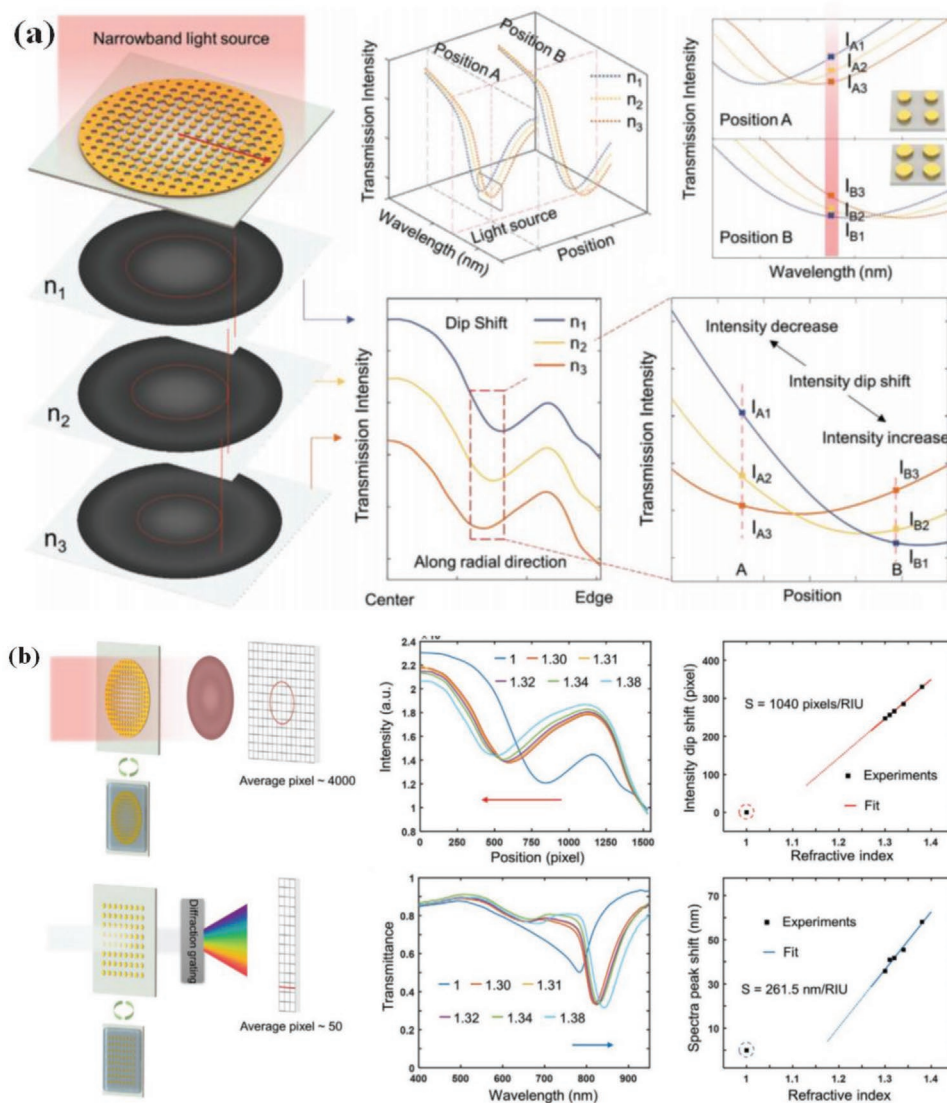

Figure 5. a) Schematic representation of spatially multiplexed imaging-based molecule sensing on the circular gradient plasmonic metasurface. b) Detailed study of the schemes of the detection limit of imaging-based sensing.[176] Reproduced with permission.[176] Copyright 2021, Wiley-VCH.

**ADVANCED
SCIENCE NEWS**

www.advancedsciencenews.com

**ADVANCED
OPTICAL
MATERIALS**

www.advopticalmat.de

RI increases from n_1 to n_3, the resonance peaks shift to longer wavelengths, resulting in a decrease in intensity at the location A and an increase in intensity at the position B. The variations in the position of intensity curve depend on the intensity variation at each position.

The tuning in the minima of the intensity pattern caused by a unit variation in the RI of the medium covering the metasurface sensor is used to assess the sensitivity of the imaging-based sensing method. As illustrated in Figure 5b, the intensity is determined as a function of radial distance from the center by averaging the intensity values of a few thousand pixels on a thin ring. Suppression of disturbances from recording and fabrication defects greatly improves the signal-to-noise ratio. To record comparable transmission pictures, a succession of RI of the liquids (with RI n ranging from 1.30–1.38) is utilized as the covering medium. If the covering material has a bigger RI, then the transmission dip moves towards the sensor center, as shown by the red arrow. The sensitivity S_m is calculated by successfully fitting the position of the dips of transmission as 1040 pixel RIU^{-1}. The limit of detection (LOD) illustrates the ratio of A/S_m, where S_m using for sensitivity and A shows the method's resolution, which is set to 1 pixel. Hence, the LOD for this novel sensing technique is 0.00096 RIU. Furthermore, the manufactured sensor can perform under a high background RI of 1.7, which covers the most detecting scenarios, according to experimental results on sensitivity and spatial range of dip shift.

The refractometric approach is an emerging effective tool for resolving the complex molecule interactions in biological and chemical systems.[177,178] Several resonant plasmonic antenna designs based on metals have been employed to obtain tailored absorption enhancement. Nevertheless, they exhibit important limitations due to the metal inherent damping.[24] Dielectric metasurfaces with low Ohmic loss comprised of various materials such as the amorphous silicon,[179,180] gallium arsenide (GaAs),[181] and the chalcogenide glasses, can be used to overcome this constraint.[182]

Leitis et al.[70] presented a germanium-based metasurface sensor that combines chemically selective broadband IR detection with angle scanning refractometric techniques' device-level simplicity along with spectrometer-free working. In particular, they used a resonator architecture of nanophotonics that produces a highly surface-sensitive and spectrally sharp resonance, with the spectral position regulated by the mid-IR light incidence angle. When there is a target with a broadband source, the angle-multiplexed device must reflect resonantly in a small spectral range at around a specific frequency ν at each θ (incidence angle) (**Figure 6**a). A dielectric metasurface made up of an anisotropic zigzag array of germanium resonators atop a calcium fluoride (CaF$_2$) substrate interacts to produce ultra-sharp reflection resonances to produce this optical response. Figure 6b shows that the developed high-Q metasurface is capable for angle-multiplexing as well as to efficiently support considerably amplified near-electric fields in the near surrounding of resonators, resulting in high surface sensitivity. The resonance line shape is significantly attenuated by near-field coupling to adsorbed analyte molecules, affecting the strength of the absorption bands.

A small sensor system, consisted of a broadband source, two mirrors on coaxially rotating arms, and a broadband detector,

can be produced (Figure 6c), owing to the immense surface sensitivity and the particular resonant reflection at certain incidence angles (θ). The intensity and the spectral position of the analyte's vibrational bands, which are connected with the imaginary component k of the complex RI, are uniquely determined by the output of such an angle-multiplexed fingerprint retrieval device, as shown in Figure 6d.

The surface sensitivity of a developed device, which comprised a thin film of the PMMA solution produced by spin coating onto a chip, was tested. After PMMA deposition, the normalized reflectance spectra demonstrated a significant depletion of the reflectance peaks, which was associated with the polymer's vibrational bands (Figure 6e). The estimated absorbance $A(\theta)$ is also plotted at the bottom of Figure 6e, which was computed from the amplitudes of peak reflectance R_0 and R_A at each angle of incidence before and after the coating of polymer using the formula $A(\theta) = \log_{10}(R_A/R_0)$ to further validate the recovered absorption signature of the deposited PMMA.

A bioassay was also performed for the sensing of human ODAM utilizing single-stranded DNA aptamers that can selectively bind to ODAM to demonstrate the developed sensor's broad spectral coverage ability to chemically detect a wide range of various analytes. The use of the bioassay based on ODAM-specific binding aptamers with the fabricated device showed that it successfully meets the demands for early, easy, and quick detection of periodontal disorders and their development. Figure 6f depicts the detection of various analytes in a higher detail.

4.2. Surface-Enhanced Infrared Spectroscopy (SEIRS, for IR <Conventional ATR>, SERS or TERS for Raman Spectroscopy)

The identification of trace organic contaminants using ultra-sensitive SEIRS is an essential issue in environmental protection. However, due to material limitations, SEIRS detection performance displays low sensitivity and poor reproducibility. Vibrational spectroscopy is an efficient alternative to refractometric sensing for molecular optical sensing that provides an effective way to identify surface-bound molecules and to obtain the specific chemical information about each particular analyte. Spectroscopic approaches, such as the IR absorption and Raman spectroscopies, enable monitoring of chemical reaction and label-free detection as well as the kinetics of interactions between analytes. Raman spectroscopy investigates molecular vibration in depth using the method of photons inelastic scattering, whereas IR spectroscopy uses light absorption measurements to retrieve chemical information. Although both of these approaches are widely established for chemical investigation, their sensitivity is severely limited due to the weak light–matter interaction in the IR spectral range and the relatively small molecule cross-section for Raman scattering. Accordingly, it is difficult to analyze low-concentration analytes with traditional spectroscopic methods. This difficulty can be solved by using SERS[183,184] and SEIRAS to exploit the nanophotonic improvement from the well-designed metasurfaces.[24,185,186] SERS and SEIRAS can be used to avoid the near-field enhancement limitation of plasmonic metasurfaces. The recent development of
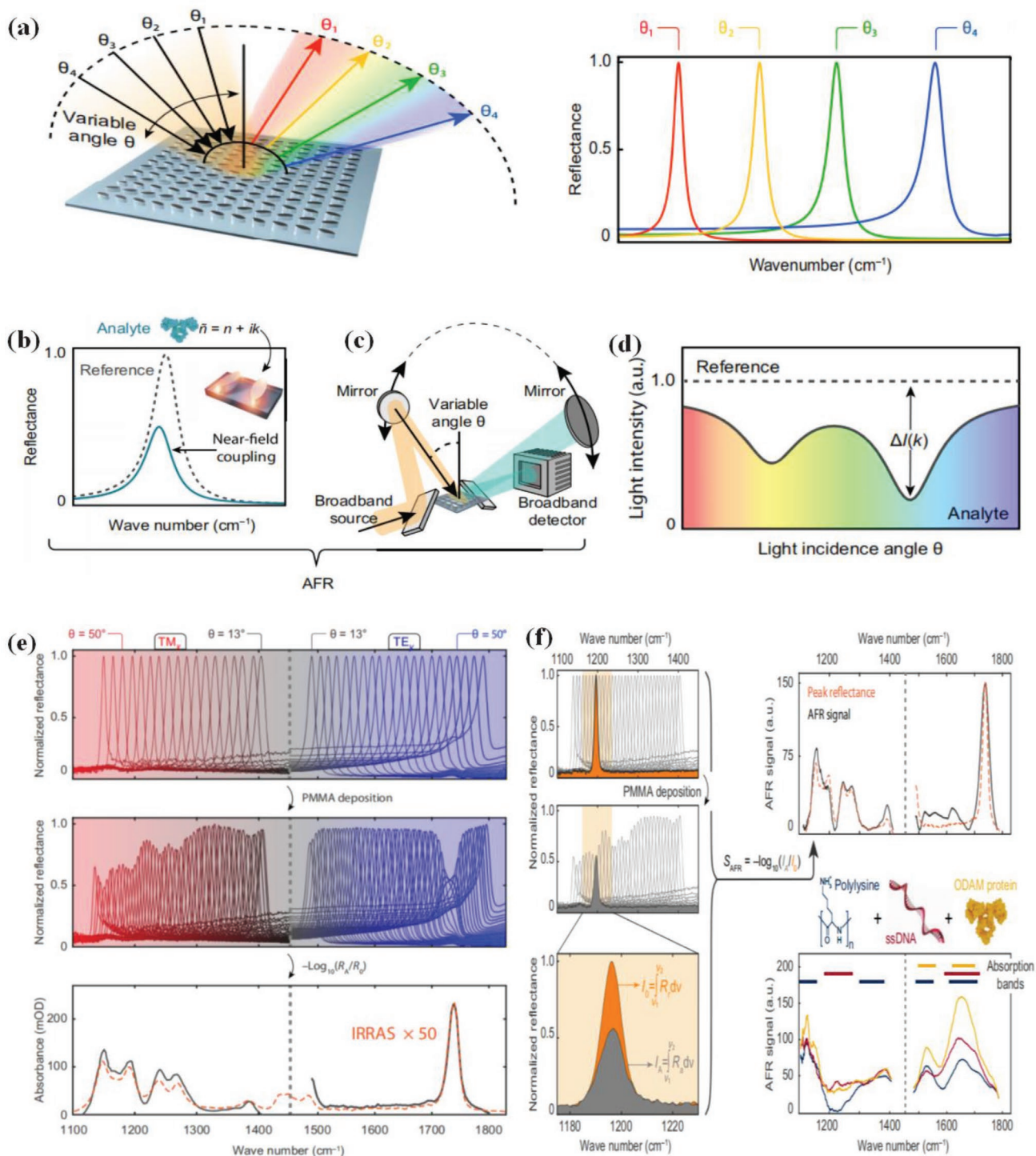
Figure 6. Broadband fingerprint retrieval via angle-multiplexing. a) A germanium (Ge)-based high Q-factor of the all-dielectric metasurface produces ultra-sharp resonances with a large spectral range and a specific resonance frequency. An angle-multiplexed setup particularly suitable for the spectroscopy of the surface-enhanced mid-IR molecular absorption is realized by continuously scanning the incidence angle, resulting in a variety of resonances throughout a target fingerprint range. b) A substantial fluctuation of the resonance line shape corresponding to the vibrational bands of absorption is caused by strong near-field interaction between the molecular vibrations of the analyte and the dielectric resonators. c) Broadband operation and device implementation are possible thanks to angle multiplexing and the spectral selectivity of the high-quality (Q) resonances. d) The device scheme's chemically specified output signal.[70] e) The metasurface's normalized reflectance spectra before and after analyte application. The angular range is $\theta = 13$–$60°$, corresponding to tuning with a broad spectral range of 1120–1800 cm^{-1} along with absorbance spectrum derived from the reflectance profile prior and later of the analyte coating expressed in the optical density (OD) units. The signal enhancement factor is roughly 50, and the matching with independent IRRAS recording is excellent. f) Detection of molecular fingerprints using angle scanning without a spectrometer and a multistep bioassay application.[70] Reproduced with permission.[70] Copyright 2019, American Association for the Advancement of Science (AAAS).

**ADVANCED
SCIENCE NEWS**

www.advancedsciencenews.com

**ADVANCED
OPTICAL
MATERIALS**

www.advopticalmat.de

the metasurfaces for SERS and SEIRS is thoroughly discussed in this section.

The SEIRA investigation of the broadly using organic electronic/optoelectronic material Tris(8-hydroxyquinoline) aluminum (III), (Alq$_3$), was initially reported by Zvagelsky et al.[187] For the SEIRA investigation of Alq$_3$ thermally deposit layers (TDL) with film thickness growth, a unique metasurface design was developed, based on arrays of the gold Y-shaped nanoantennas. This design allows each metasurface to have two distinct plasmonic resonances, allowing the accurate investigation of several vibrational modes of a molecule laid on a single substrate. The manufactured metasurfaces' near-field enhancement exhibited saturation and a loss of signal as the analyte layer thickness increased from half the height of gold nanoantennas onwards. **Figure 7**a schematically illustrates the spectrum calculation and polarization direction as well as the relative absorbance of Y-shaped nanoantennas for various thicknesses of aluminum oxinate and the molecular plasmonic coupling with $d = 65$ nm. The purple line depicts the analyte's antenna absorbance, whereas the gray line depicts a close image from the ATR transmittance spectrum of the Alq$_3$ powder. The dips in the Alq$_3$ transmittance spectrum clearly coincide with the dips in the near-field enhanced plasmonic absorption spectrum with the same line width and frequency as reported previously.[188]

Furthermore, using large-area templates (cm^2) based on self-organized (SO) NR antennas; the capability of very sensitive SEIRA spectroscopy was demonstrated. More specifically, Giordano et al.[25] described the engineered extraordinarily dense arrays antennas of gold NR with polarization-sensitive LSPRs, which are controlled in a wideband ranging from near-IR to mid-IR spectral region, and are overlapped, with the window of so-called "functional group".

Figure 7b shows an atomic force microscope (AFM) profile and a cross-sectional image of the aligned glass NRs developed by defocused ion beam irradiation, as well as a mid-IR spectrum of relative optical transmittance of the two various samples of the Au NRs arrays with a self-assembled monolayer of ODT molecules and vibrational signals from the ODT monolayer. The ODT molecule's distinct vibrational modes peaking at 2850 and 2918 cm^{-1} attributed to symmetric and antisymmetric stretching modes of the functional group CH$_2$, respectively, while peaks at 2877 and 2960 cm^{-1} corresponds to symmetric and antisymmetric stretching modes of the functional group CH$_3$, respectively. The signal detected with an IR optical microscope (blue line, 100 µm optical spot) is compared to the signal detected with a standard IR spectrometer shown in black line with optical spot of 3 µm size.

More interestingly, by using the developed self-assembled monolayers of the IR-active ODT molecules, the polarization-sensitive SEIRA was established, which was homogeneous over the macroscopic region and stable over time. In SEIRA, typical Fano resonances are produced due to the strong connection between the plasmonic excitation with molecular stretching modes. The active hotspots in the arrays were SO engineered, resulting in a 5.7% increase in signal amplitude. This result is comparable to that of lithographically manufactured nanoantennas (NAs) and remains stable as the optical excitation point shifts from micro to macro-scale, allowing highly sensitive SEIRA to be achieved using low-cost nanosensors.

Similarly, a highly controllable approach for fabricating periodic bowtie SERS substrates with a narrow nanogap, high SERS enhancement, and a good homogeneity over a vast area was reported in our earlier work.[2] To create a conductive plasmonic bowtie array, the periodic bowtie template is first produced over a gold film using holographic lithography (HL). Figure 7c depicts a schematic representation of the fabrication. The gap is subsequently narrowed using pulsed Ag electrodeposition, while electrochemical dark-field spectroscopy is used to measure the gap in situ. As a result, the most sensitive change in the scattering spectra, just as the gap is ready to merge, was detected, resulting in uniform SERS substrates with gap sizes as small as 5 nm. The average enhancement factor was 5×10^7 to 1×10^8, which is 50 times greater than that obtained from Au NP-assembled substrates and 140 times greater than that produced from commercial Klarite chips (Figure 7c, bottom). This substrate has a great prospect for SERS applications in the real world.

The most traditional surface-enhanced sensing relies on plasmonic metasurfaces based on metallic antennas. However, they have substantial constraints in terms of lossy materials and CMOS compatibility for mass production. Dielectric resonators are a viable choice for electric and magnetic field control over a wide frequency range. Metasurfaces made up of arrays of dielectric resonators can reveal additional functionality for applications such as generalized phase control and flat optics. Tittl and colleagues recently demonstrated a unique mid-IR spectroscopy method that uses a pixelated dielectric metasurface to spatially encode molecular absorption signatures into chemical-specific 2D barcodes.[71] They created an imaging-based nanophotonics technology for efficiently sensing mid-IR molecular fingerprints, which are utilized to identify and analyze surface-bound analytes chemically. Furthermore, the suggested specified chemical approach can resolve the absorption fingerprints without the use of spectrometry, moving mechanical parts, or frequency scanning, opening the door for sensitive and adaptable tiny mid-IR spectroscopy instruments.

The fabricated design takes into account the use of Mie type resonances collective nature, also known as super-cavity modes, which are driven by the bound state in the continuum (BIC) physics.[189] In addition, the designed high-Q resonances have no additional resonance noise and are spectrally clean. This is very important because it enables extremely highly spectrally selective augmentation of the chemical fingerprint's spectroscopically rich information.

The identification of molecular fingerprints using a monolayer of recombinant protein A/G was thoroughly investigated. The spectra of the metapixel reflectance were obtained prior and later to the protein A/G interaction. **Figure 8**a show the outcome of this experiment. The characteristic amide I and II absorption signature of the A/G molecules of protein are revealed (Figure 8b) by the absorbance signal computed from the peak of reflectance before (R_0) and after protein interaction (R_S), which is in perfect match with an independent IR reflection–absorption spectroscopy (IRRAS) recording. Furthermore, the integrated reflectance signal from the spectrum data of each metapixel was calculated, allowing the thorough assessment of the capabilities of the designed metasurface sensor for imaging-based spectrometerless fingerprint identification.
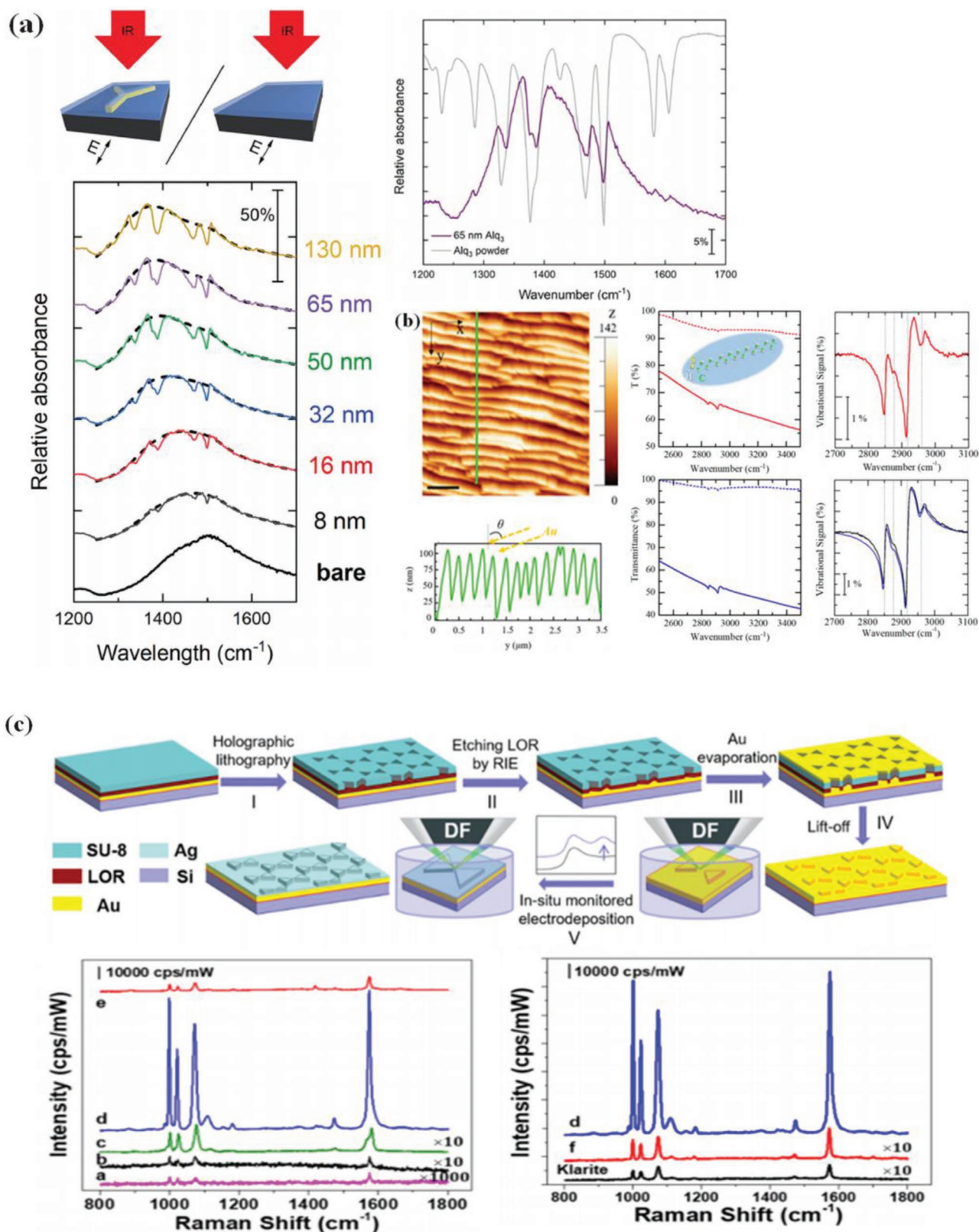
Figure 7. a) Diagram of spectrum calculation and polarization direction with relative absorbance spectra of y-shaped nano-antennas of various thicknesses and comparison of powder samples with $d = 65$ nm.[187] b) AFM topography profile and cross-sectional image of a high-aspect-proportion of the rippled glass template with vibrational signals extracted from mid-IR relative optical transmittance (*T*) spectra of two different samples of Au NR arrays functionalized with a self-assembled monolayer of ODT molecules.[25] c) Illustration of fabrication methods with SERS performance and comparison of several metagrating designs.[2] Reproduced with permission.[2,25,187] Copyright 2020 and 2021, American Chemical Society.
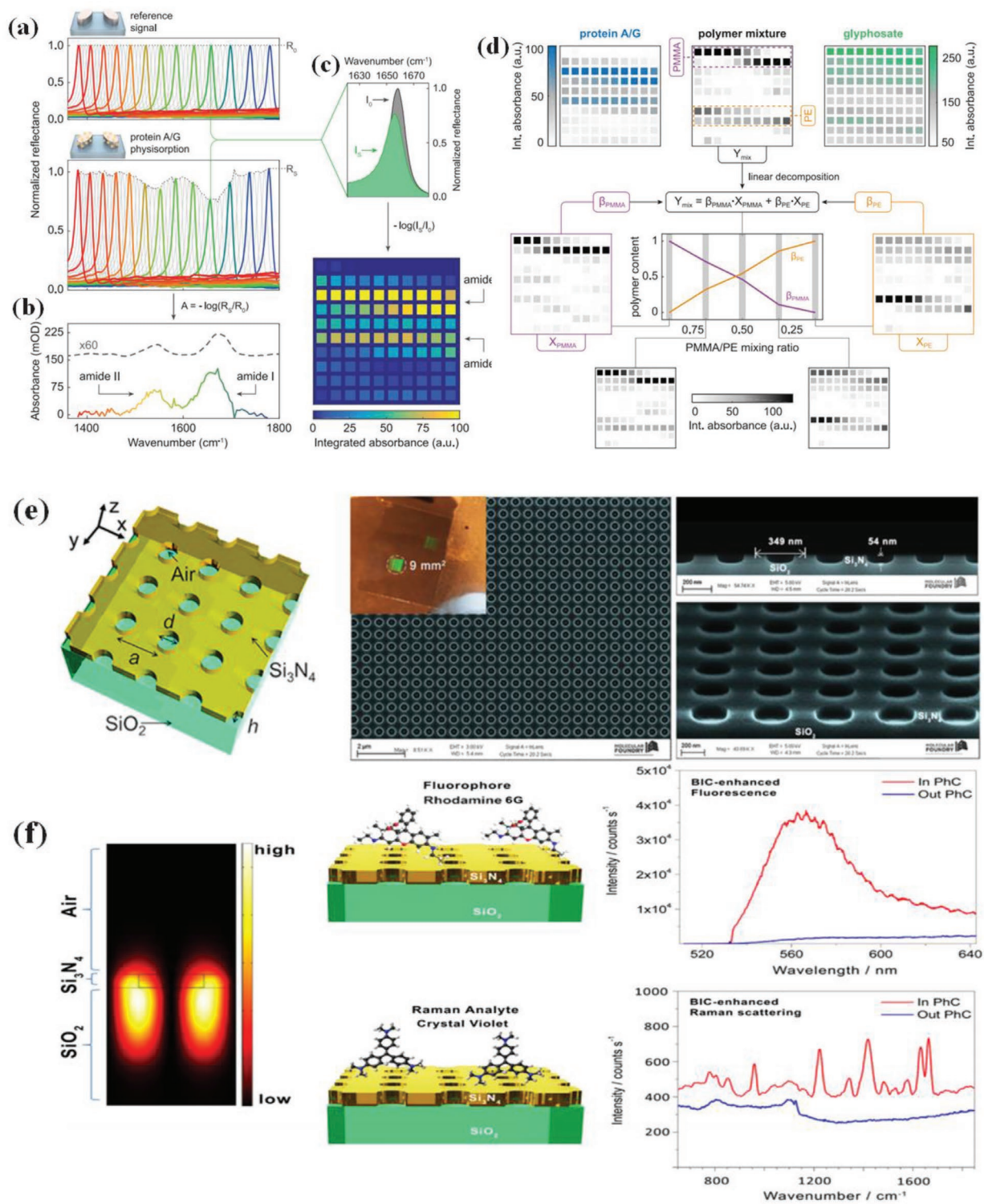
Figure 8. Retrieval of molecular fingerprints and mapping of the particular absorption, a) normalized reflectance spectra with metapixel of the monolayer of protein A/G before and after physisorption. b) Absorption of fingerprints of protein estimated from the reflectance profiles of R_0 and R_S compared to the measurement of an independent IRRAS. c) The metasurface's broadband spectrometerless functioning can be reproduced by integrating the reflectance signal of all the pixels with spectral integration, which converts the absorption signature. d) Chemical identification and compositional analysis using imaging.[71] e) Schematic illustration of design and fabrication with SEM images, and f) the electric field with resonance condition, schematic arrangement of the PhCM, fluorescence, and CV molecule Raman scattering.[190] Reproduced with permission.[71,190] Copyright 2018, AAAS and Copyright 2021, American Chemical Society.

**ADVANCED
SCIENCE NEWS**

www.advancedsciencenews.com

**ADVANCED
OPTICAL
MATERIALS**

www.advopticalmat.de

These integrated signals are employed to compute the signals of metapixel absorbance via the formula $A = -\log(I_S/I_0)$, which are then resized from 0 to 100, and are analogous to the optical response of metasurface with a wideband detector prior (I_0) and after (I_S) deposition of the protein layer (Figure 8c).

More interestingly, imaging-based chemical identification and compositional analysis were performed on the molecular barcodes of protein A/G, a combination of PE polymers and PMMA, as well as glyphosate pesticides. As shown in Figure 8d, the analytes' different absorption fingerprints were revealed. The barcode matrices for the PE polymer/PMMA mixture with various contents were confirmed with reliable readout.

The surface EM states with particular localization, dispersion characteristics, and high-field intensity that approximate surface-plasmon resonances while suppressing the Ohmic losses in metals are of tremendous interest. However, dielectric nanoantennas can only provide limited alternatives in the visible range of optical frequencies. Romano et al.[190] developed all-dielectric metasurfaces whose design consists of transparent silicon nitride (Si−N) based nanostructured supporting BICs. It was shown that the design of specific type of Fano type resonances can be successfully employed in regular microscopy for practical purposes. The far-field intensities of fluorescence emission and Raman scattering of molecules scattered on these metasurfaces were both boosted by ≈103 times. Furthermore, resonant matching of the LSPR with the BIC field is observed, and the gain of traditional SERS signals was improved by more than one order of magnitude. Enhanced sensing, nonlinear mechanisms, and Raman imaging, were also important benefits.

The schematic arrangement of the design production of 2D square photonic crystal metasurfaces (PhCMs), as well as the top-sight, side-sight, and tilted-sight scanning electron micrographs (SEM) of a PhCM sample, are illustrated in Figure 8e. A snapshot of the large-area PhCM is shown in the inset. Figure 8f shows the numerical simulation results of the intensity of electric field inside the unit cell in resonance settings, as well as a schematic illustration of the PhCM with R6G fluorophores coated across the entire sample surface and R6G molecules' fluorescence emission spectra. The PhCM schematic arrangement is shown in the same figure (Figure 8f), with CV Raman analytes coated throughout the entire sample and the spectra of surface Raman scattering of the CV molecules inside and outside of the PhCM. In the air, the resonant mode creates a strong near-field enhancement in the region near to the surface as it decays exponentially. When the RI of the material sample above the PhCM grows, the resonant wavelength shifts to a longer wavelength, which can be employed for sensing.[191,192] In comparison to the surrounding un-patterned Si_3N_4 film, the characteristic intensity of fluorescence emission was magnified by a factor of ≈40 inside the PhCM. Multifold raster scans of an area as large as the entire PhCM were used to confirm this. In this experiment, crystal violet (CV) dye molecules were used as probe Raman analytes. For comparison purposes, the BIC-enhanced Raman spectra stimulated on the PhCM are shown alongside the spectrum outside the structure. On the un-patterned silicon nitride, there was negligible Raman scattering.

4.3. Surface-Enhanced Thermal Emission Spectroscopy (SETES)

The approach of SES based on plasmonic metasurfaces and nanoantennas aims at lowering the detection limit for biological sensing. IR spectroscopy is a good method for identifying molecular species, but it requires an IR light source, which is often expensive. The TE of III-V type semiconductor metasurfaces is another type of SES approach. More intriguingly, the existence of a chemical species attached on the surface affects the emission spectrum in a similar way whereby SEIRA spectroscopy modulates the emission spectrum. The boosting of EM field attained with a plasmonic metasurface is used to detect the molecular species' vibrational fingerprint. Owing to the fact that the metasurface serves as both source of radiation and sensor chip at the same time the experimental setup is reduced, making it more compact, reliable, and promisingly cost-effective. Surface-enhanced TE (SETE) spectroscopy is a revolutionary technique for molecule sensing that is intriguing for miniaturized and integrated devices.

Barho et al.[193] described a new spectroscopic technique based on the spectroscopy of TE at a temperature of 65 °C for molecule detection. The plasmonic metamaterial, like plasmonic metasurfaces or nanoantennas used for SEIRA, serves two purposes. It acts as an emitter to successfully substitute the source of IR radiation and it efficiently boosts the signal of the analyte molecule. **Figure 9**a shows the meta-grating patterned thermal emitter as well as a scanning electron microscope picture and a schematic illustration of the emission spectroscopy experimental setup. Figure 9b shows the empirically determined metasurfaces TE (MTE) in parallel and perpendicular polarization orientations to the grating. The reflectance for the same polarization direction is also presented for comparison purposes. Kirchhoff's law was expressed since the MTE is opaque at frequencies lower than 1700 cm⁻¹

$$\varepsilon(\nu) = 1 - r(\nu) = \alpha(\nu) \tag{3}$$

where $r(\nu)$ represents the MTE's reflectance, while $\alpha(\nu)$ is its absorbance. Because the sample is only a little warmer than the room temperature (RT), the reflectance and the emission extrema are at the same wavelength. In contrast, when the emission is measured at high temperatures, the dielectric function significantly changes with variation in temperature, causing a gap between the reflectance and emission extrema.[194,195]

By collecting light polarized parallel and perpendicular to the grating ridges, the TE of an MTE with a PFTMS layer was recorded. The functionalized MTE's emittance is compared to the untreated MTE's reference in Figure 9c. The existence of a molecular layer is evident at ≈1000 cm⁻¹ in the spectrum of photons polarized perpendicularly to the grating (Figure 9c). Because of their hybridization, both resonances have plasmonic properties. The spectral alteration may be traced back to the existence of PFTMS's very high absorption bands in IR at around 991, 1025, and at around 1079 cm⁻¹ and the resultant large changes in the real component of the RI of PFTMS, according to the Kramers–Kroning relation. The band at around ≈1079 cm⁻¹ in the IR spectra of PFTMS sample is attributed to Si−O−CH₃. On the other hand, the grafted PFTMS layer has negligible effect on the spectra in the opposite polarization
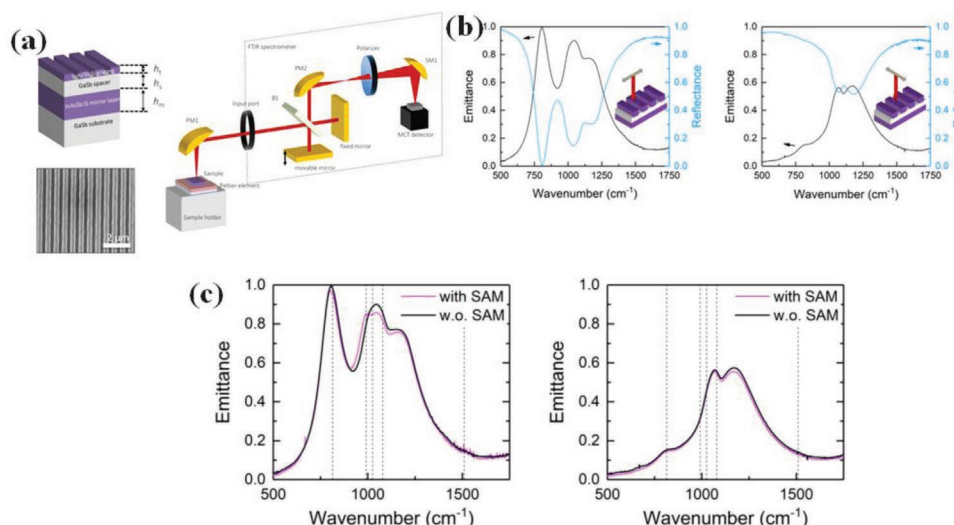
ADVANCED
SCIENCE NEWS

www.advancedsciencenews.com

ADVANCED
OPTICAL
MATERIALS

www.advopticalmat.de

Figure 9. a) Schematic illustration and experimental setup of the perfect absorber metamaterial with scanning electron microscopy images, b) emittance and reflectance spectra with radiation polarized perpendicularly and parallel to the grating, and c) reflectance spectra of the metamaterials with and without deposition of PFTMS layer in polarization perpendicularly and parallel to the grating.[193] Reproduced with permission.[193] Copyright 2019, Journal of the American Chemical Society.

direction. The "quarter wavelength" of the emittance peak gives not enough enhancements of strong field that is needed to achieve a sensitivity that provides detection of a modification caused by a molecular layer without the hybridization effect and plasmonic field enhancement.

The TE of the objects is typically spectrally wide, unpolarized, and stable over time. The new nanophotonic structures and concepts that allow the on-demand active modulation of the TE process challenge these beliefs. This brings up numerous new possibilities in chemistry, thermal management, health care, sensing, imaging, and spectroscopy.

4.4. Chiral Molecule Sensing

Chirality is a type of geometric symmetry of the objects. It causes important chemical and physical properties and it is significantly important in cell communication, protein function, and human physiology in general. More specifically, the word chirality is derived from the ancient Greek "$\chi\epsilon\iota\rho$" (pronounced as "kheire"), which means "hand" that is a common chiral item. A chiral item or system is different from its mirror image. Thus, it cannot be superimposed onto it. Many naturally occurring biomolecules and medicines, known as enantiomers, exist in both the left- and the right-handed versions. Enantiomers manifest totally different metabolic absorption, therapeutic promising, and toxicological consequences. Chiral-molecular structural anomalies have been found to play a significant role in the development of neurodegenerative and neuropsychiatric illnesses such as Alzheimer's and Parkinson's disease.[196–198]

Chirality can exhibit itself in physical aspects in addition to geometrical concerns. In crystallographic ordering, chemical bonding, and other features determined by the electrical structure, symmetry is a crucial feature for every practical physical system.[199] For instance, the "chiral state" of light can present itself optically as a distinct response to right- or left-handed circularly polarized (RCP and LCP, respectively) light. For those two polarization states, a chiral material has different complex refractive indices.[200] CD is caused by a difference in the imaginary part, which results in various absorption of RCP and LCP light. When light travels through a chiral medium, a linearly polarized light field is rotated with regard to its original orientation. The difference in the real component of the RI can explain this effect, which is known as optical rotatory dispersion (ORD). A superposition of the LCP and RCP light is termed as a linearly polarized light field.

The CD and ORD spectroscopies are important methods in various fields, like biology, physics, chemistry, and medicine, for investigating chiral molecules of various types and sizes, and notably for assessing macromolecule secondary structure and conformation.[201] CD and ORD measurements were extensively utilized to determine the structural, kinetics, and thermodynamic features of macromolecules. However, the optical response of the most chiral molecules is usually very weak, and therefore it is difficult to analyze the above features in small volume analytes using CD and ORD spectroscopies.

Metasurfaces can efficiently enhance the light–matter interaction in the phenomenon of chiral sensing by generating a superchiral field with high optical chirality concentrations, C, defined as

$$C\{E,H\} = \frac{-k_0}{2c_0}\text{Im}\{E \cdot H^*\} \qquad (4)$$

In Equation (4), the wavenumber and the characteristic speed of light in the free space are represented by k_0 and c_0, respectively, and the complex electric and magnetic fields are represented by E and H, respectively.[202]

In order to improve and elucidate the essential parameters in the design, Mohammadi et al.[202] developed an analytical model to investigate the correlation between the performance and characteristic features of an arbitrary metasurface. The

conditions for obtaining the chirality detection with excellency with the platform of nanophotonic, as defined by the analytical model, are as follows: 1) Consideration of the attenuation role of the sensing device's chiral absorption in removing the background signal; 2) reduction of permittivity influence of the overall output signal, using the same factors of intensity enhancement for the right and the left CPL; and 3) optimization of the output signal by using high optical chirality. As a result, metasurfaces can be constructed and provide EM fields that are strong, homogeneous, and easily accessible for efficient C intensification. Furthermore, current research suggests that the dissymmetry factor or parameter is also a crucial element when fabricating chiral metasurfaces to improve system's chiral sensing capabilities.[203,204]

Biomolecular sensing, which recognizes genetic fragments and proteins, has recently been considered in cancer and infectious disease diagnostic techniques. Nanomaterials capable of controlling the light–matter interaction at the scale of single nanometer (nm), where proteins and genes bind directly to the receptors, have been developed. Palermo et al.[205] demonstrated numerically that the interface between a chiral metasurface and hyperbolic metamaterials (HMMs) can provide both high sensitivity and specificity for nucleic acids and proteins with low molecular weight. Hyperbolic dispersion (HD) metamaterials enable molecular biorecognition with extraordinary sensitivity thanks to coupled and highly restricted plasmon polaritons.

Specificity is entirely determined by the receptor–ligand interaction at the in-plane sensing surface. A modified chiral metasurface with out-of-plane allows the HMM sensor to perform three critical functions. Helicoidal metasurfaces can act as 1) efficient diffractive elements to excite surface and bulk plasmon polaritons, 2) out-of-plane sensing branches to reduce the diffusion limit and increase the sensing surface, and 3) biorecognition assays via CD and chiral selectivity.

The schematic diagram of type II HMMs arrangement composing of alternating metallic and dielectric thin films is shown in **Figure 10**a (above). A right-handed Au helix with the geometrical properties depicted in Figure 10a (below) was used to make the single unit cell. The wire radius (r), helix radius (R_h), pitch height or axial pitch (p), the number of pitches (N_p), and the lattice constant (a) are all included in the helix array. It was observed that the bulk plasmon polariton modes of the underlying HMM can be excited by the chiral metasurface hypergrating (CMH). The frequency of these modes is expected to fluctuate as a function of the concentration of the analytes bound to the metasurface, indicating the sensing platform's sensitivity. As a result, the ultralow molecular weight of various molar fractions of an aqueous solution of 1,2,3-propantriol ($C_3H_8O_3$) was determined. Koohyar et al. provided the RI fluctuations for various molar fractions of this solution.[206]

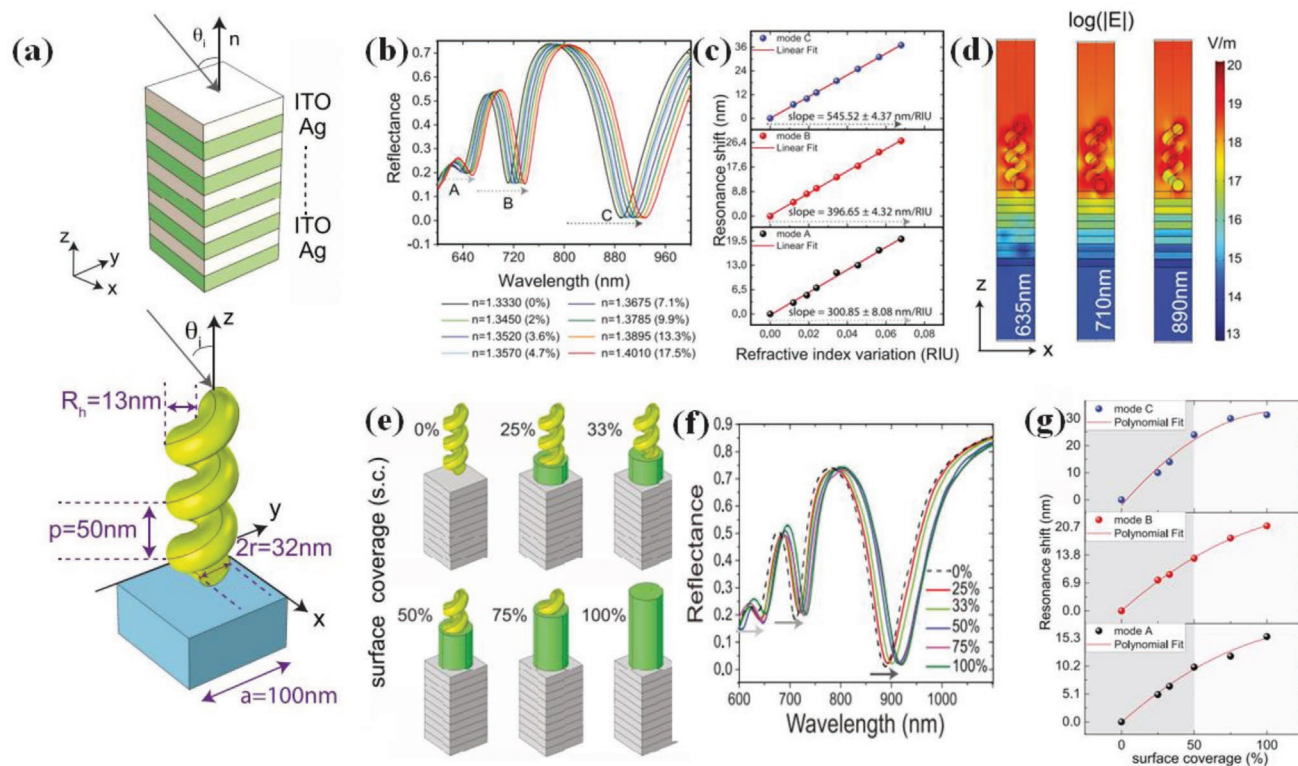Figure 10b illustrates the predicted reflection spectra of the designed CMH-HMM-based sensor for sensing various

Figure 10. a) The essential structure properties of one lateral unit cell of the out-of-plane chiral structure made of a right-handed Au helix on a glass substrate are shown in the ITO/Ag HMM schematic. b) Performance of the CMHHMM sensor evaluation: computed reflectance spectra with varied mol concentration of 1,2,3-propantriol in the distilled water. c) Wavelength attenuation in resonance for the modes of A, B, and C as a function of the RI change and linear fitting, and d) in the logarithmic scale, XZ maps of the intensity of electric field via the CMHHMM structure for the three various modes. e) Illustration of the simulated design with various proportion of surface covering. f) The reflectance spectra and g) the resonance wavelength tuning for various modes, A, B, and C, as a function of surface coverage.[205] Reproduced with permission from.[205] Copyright 2020, American Chemical Society.

**ADVANCED
SCIENCE NEWS**

www.advancedsciencenews.com

**ADVANCED
OPTICAL
MATERIALS**

www.advopticalmat.de

concentrations of 1,2,3-propantriol solutions. It was discovered that the RI ranged from 0 to 0.068, which corresponded to a molar ratio of $C_3H_8O_3$ at about 17%. As expected, as the RI increases, the calculated reflectance minima (mode dips) of the coupled system shifts linearly towards longer wavelengths (Figure 10c). This shift can be interpreted as a measure of the system's sensitivity to the analyte.

The ratio of the change of RI (Δn) of the solution of the sample flowing on sensor's top to the wavelength shift ($\Delta\lambda$) of the sensor resonance is shown in the Equation (5):

$$S = \frac{\Delta n}{\Delta \lambda} \qquad (5)$$

For the first mode, A (635 nm), S_A reached 3.3×10^{-3} RIU nm^{-1}, and $\Delta\lambda_A = 20$ nm, while S_B is seen to be 2.5×10^{-3} RIU nm^{-1}, and $\Delta\lambda_B = 26$ nm for the second mode, that is, B (710 nm). Similarly, $S_C = 1.8 \times 10^{-3}$ RIU nm^{-1}, and $\Delta\lambda_C = 37$ nm for the C (890 nm) mode respectively. The associated LOD (limit of detection), which is equal to 0.0015, is the smallest RI fluctuation that can be recognized (the shift is 1 nm when considering normal nanofabrication structural tolerance). The appeared variance in the sensitivity between the three modes of sensor is attributed to various $\Delta\lambda$ in all three cases. Mode C outperforms the other two modes in terms of sensitivity. This is because of the highly limited field distribution on the superstrate (Figure 10d) at HD and the evidence that the field's transverse decay markedly varies from one mode to the next in the HMM.

The wavelength shift of the BPP modes is proportional to the number of molecules that bind selectively on the surface of the helices. To numerically simulate this effect, various percentages of the helicoidal structures' surface coverage were considered, from the bottom to the top of the helices (as illustrated in Figure 10e), with the maximum fluctuation of the considered RI (0.0680) only influencing the covered region surrounding the helix. It must be noticed that the RI changing was only evaluated in a cylinder around a single helix, but n was not observed in the bulk. Therefore, two situations were considered, 0% surface coverage (s.c.) and 100% s.c., in which molecules completely cover the whole surface of the helix. In the latter case, the highest spectral variation was observed to be 15, 21, and 31 nm for mode A, mode B, and mode C respectively. Similarly, four-intermediate partial s.c. situations of 25, 33, 50, and 75% were also considered (Figure 10f). The variation tends to saturate around the bulk RI sensitivity as the volume of the cylinder increases (Figure 10c) to 100% s.c.

At the same time, the smallest detectable s.c., which corresponds to the minimal surface coverage required to have a noticeable variation of all the three modes, can be also determined. The results shown in Figure 10g reveal that all the three modes shift by at least 1 nm for an s.c. of about 16%, whereas the observed highest sensitive mode C tunes by 1 nm with a surface coverage of about 12%. This allows the calculation of the bulk sensitivity, a crucial metric used to define the performance of a bio/molecular sensor that is highly connected to surface coverage. The mass sensitivity for the given system is 0.04 pg mm^{-2}.

Sensing molecule chirality at the nanoscale has been a long-standing challenge due to the inherently weak nature of chiroptical signals. Nanophotonic techniques have been effective in accessing these signals. Yet, it has not been achieved complete sensing of the chiral part of the molecule's RI (magnitude and sign of both the real and imaginary parts) in most circumstances, because the faint chiroptical signals are obscured by the powerful intrinsic signals from the nanostructures themselves. Unlike plasmonics, dielectric nanoresonators have a strong response to both the magnetic and electric fields of light, making dielectric metasurface a promising alternative for chirality improvement. Droulias et al.[207] suggested a dielectric metasurface as a solution to these issues. Furthermore, it enables complete measurements of the whole chirality, it clearly distinguishes the influence of the real and the imaginary part, and it provides absolute chirality measurements, thanks to the use of a critical signal reversal (excitation with reversed polarization) that allows measurements of chirality without the need of sample removal. **Figure 11**a schematically represents a metamaterial system. The system comprises a thin slab of dielectric that successfully supports the continuous dispersion TE (components H_x, E_y, H_z) and TM (components E_x, H_y, E_z) modes of waveguide (Figure 11b). That study focused on TE_0 and TM_0 as well as on the lowest order waveguide modes, and exploited their dominant field components, that is, E_y and H_y, to build the electric/magnetic-moment pair.

As demonstrated in Figure 11c, a linearly polarized pulse is employed to excite the sample at normal incidence from the substrate side. As a result, when the incident magnetic field (H-field) is parallel to the wires (H = $H_y\hat{y}$), only the TM_{20} mode (components E_x, H_y, E_z) is excited, but it cannot couple to the orthogonal TE_{20} mode unless the chiral layer offers an essential mode-coupling. Similarly, an incident field with E = $E_y\hat{y}$ will only pair to the TE_{20} mode (components H_x, E_y, H_z). To determine the effect of chirality on the incident wave, Figure 11c shows the transmittance plot and analyzes the transmitted wave's polarization in terms of ellipticity (η) and rotation (θ). Starting at $w_m = 60$ nm, the TE_{20}–TM_{20} spectral separation decreases as w_m increases, resulting in the enhancement of the values of η and θ in the region of far-field, which are maximal at $w_m = 80$ nm, where the two modes are aligned spectrally. Increased w_m causes modes detuning, resulting in weaker signals.

Apart from physical information, the current analytical model also quantifies the system's total response. The fitted simulated results for aligned modes, where the augmentation is the greatest ($w_m = 80$ nm), are shown in Figure 11d. At $\kappa = \pm 10^{-5}$ and $\kappa = \pm 10^{-5}$i, the chiral-influencing absorption and refraction were also investigated. Consequently, the current model system allows the calculation of both the real and the imaginary parts of κ and the identification of their effect using various chiroptical signals. The coupled oscillator model confirmed this, and despite its simplicity, it successfully reproduced the numerical simulations. In **Table 1**, the performance of metamaterials and metasurfaces of various sensors is summarized.

5. Future Perspectives and Challenges

Although metasurfaces have outperformed the traditional sensing methods, there is still space for improvement.[210] The device
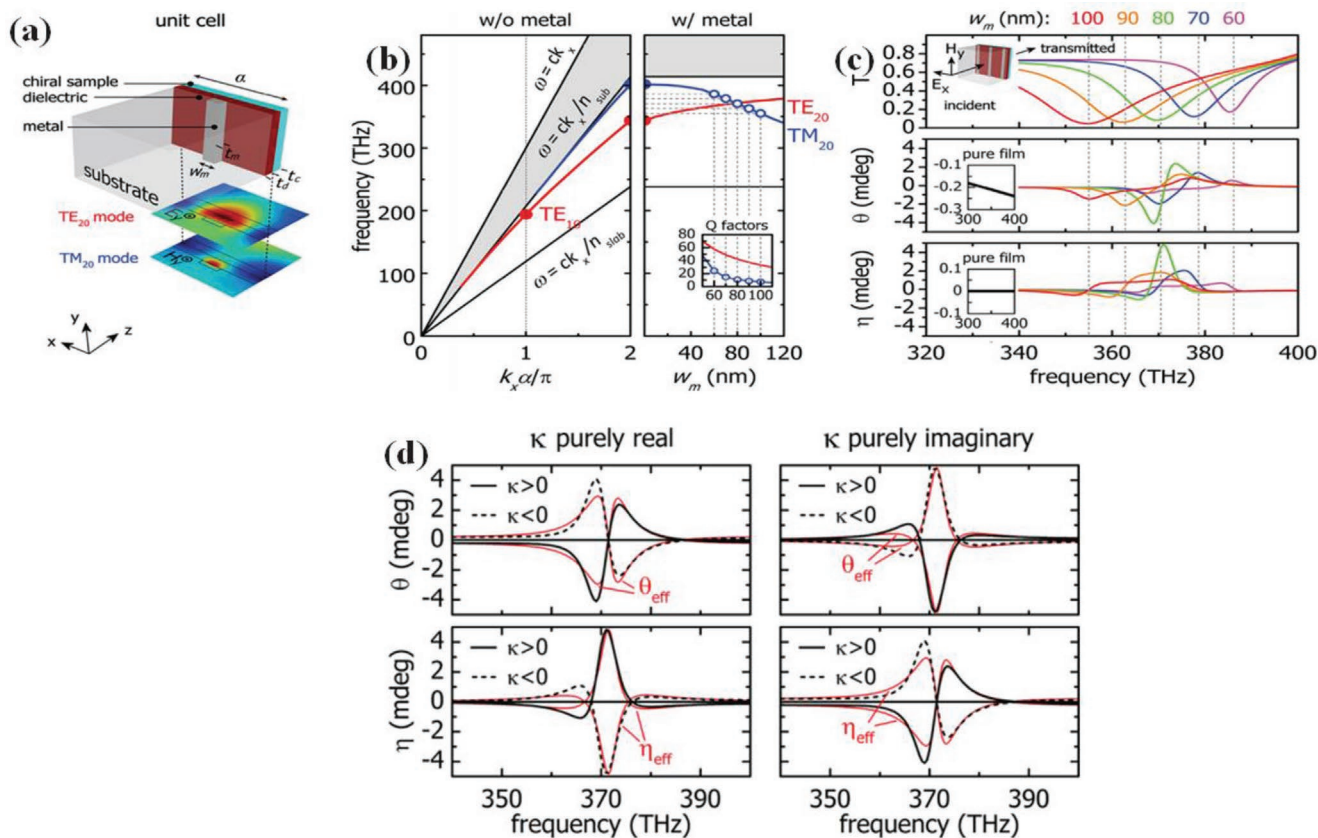
**ADVANCED
SCIENCE NEWS**

www.advancedsciencenews.com

**ADVANCED
OPTICAL
MATERIALS**

www.advopticalmat.de

Figure 11. Enhanced chiral sensing with a dielectric metasurface. a) The metasurface's one-unit cell (periodicity a). b) Left panel: in the absence of metal, dispersion of the dielectric slab's lowest order TE_0 (red line) and TM_0 (blue line) modes. c) Transmittance spectra and improved far-field chiroptical signals for a system with $a = +10^5$ as a function of TE_{20}–TM_{20} spectral alignment under TM excitation. The TM_{20} mode is excited by the TM-polarized incident wave and the chiral layer enables coupling with the TE_{20} mode. d) Improved detection of complete chirality.[207] Reproduced with permission.[207] Copyright 2020, American Chemical Society.

Table 1. Summary of metamaterials and metasurfaces sensors.

Application	Detection sample	Sample type	Nanostructure	Performance	Reference
Refractometric sensing	CO_2	Gas	All-dielectric nanodisk array and photonic crystal slab	20 ppm	[170]
Refractometric sensing	Streptavidin-biotin binding	Small molecule	Gradient Au nanorods array	15 nM	[173]
Refractometric sensing	Mouse IgG	Protein	Elliptical zigzag array	3 molecules per μm^2	[208]
Refractometric sensing	Single layer of Al_2O_3	Molecule	Gradient nanopillars and nanoholes array	1 angstrom	[209]
Refractometric sensing	DNA aptamer-human odontogenic ameloblast associated protein binding	Protein	Elliptical zigzag array	3000 molecules per μm^2	[70]
Surface-enhanced infrared spectroscopy	Organic optoelectronic material Tris (8-hydroxyquinoline) aluminum(III) (Alq$_3$)	Molecule	Gold Y-shaped nanoantennas arrays	8 nm	[187]
Surface-enhanced infrared spectroscopy	Protein A/G monolayer	Protein	Elliptical zigzag array	2130 molecules per μm^2	[71]
Surface-enhanced infrared spectroscopy	Biphenyl-4-thiol	Molecule	Photonic crystal metasurface	1 nm	[191]
Surface-enhanced infrared spectroscopy	Protein	Protein	Photonic crystal metasurface	66 nM	[192]
Surface-enhanced thermal emission spectroscopy	11-pentafluorophenoxyundecyltrimethoxysilane	Molecule	Nanograting arrays	2 nm	[193]
Chiral molecule sensing	α-Synuclein fibrils	Protein	Gold nanorods	80 nM	[196]

**ADVANCED
SCIENCE NEWS**

www.advancedsciencenews.com

**ADVANCED
OPTICAL
MATERIALS**

www.advopticalmat.de

sensitivity will be improved by developing unique fabrication design and synthesis methodologies for efficient metamaterials. At the moment, plasmonic metasurface-based sickness diagnosis is limited to serum, which needs a lengthy preprocessing procedure in a competent laboratory prior to detection. However, if POCT (point of care testing) is required, a more accessible sample containing whole blood or even sweat, saliva, and urine may be preferable. This will also make portable medical applications for health diagnostics more difficult. The advancement of optical technology will lead to more flexible and wearable devices.

Plasmonic biosensing can be employed in wearable devices to detect complex samples in real-time. However, a specific step is still required for commercially plasmonic metasurfaces' immediate detecting equipment. In the future, it may be required to meet the challenge of large-scale plasmon chip production while keeping cost under control, which will effectively promote the commercialization. On the other hand, choosing a unique metamaterial is another way to improve detection efficiency while lowering commercial cost.

The breakthroughs in nanofabrication technology resulted in the development of static meta-devices. Metasurfaces will be created by using a number of developing approaches and innovative design, which will allow low-cost, large-area, and the mass-production approaches. Tunable or reconfigurable metasurfaces will also lead to fascinating and diverse functions in a broader spectrum of applications using new functional materials, such as liquid crystals, phase-change materials, and 2D materials.

Dielectric metasurfaces can manifest designing on-demand features because of the extra degrees of freedom in the optical responses and the particular light–matter interactions. Nevertheless, there are still several problems. One of them is to establish a standard process for fabricating several types of the dielectric metasurface sensors in a large scale. Despite the recent development in the efficient manufacturing of metasurfaces, there is still no technique that is compatible with conventional semiconductor fabrication techniques. Fabrication of large-area flexible metasurfaces for high sensitivity is another important issue. Results of recent research show that dielectric metasurfaces have adequate sensitivity. Nonetheless, the overall performance is not as good as that of their state-of-the-art plasmonic equivalents. There is space to improve device sensitivity, especially for SERS. Furthermore, progress in materials science will contribute to the improvement of dielectric metasurfaces and widen their application in novel devices. Multifunctional metasurfaces, which exhibit an ability to create near-field enhancement and to operate as on-chip light sources, which can be created for the integration of ultra-compact sensor by employing active materials, such as GaN and GaAs. Moreover, several unusual materials, such as HI chalcogenides and perovskites, have recently been used in metasurfaces to obtain unique optical features. Further research on metasurface materials may lead to high-performance optical molecular sensors.

6. Conclusions

The current progress on metasurfaces was thoroughly reviewed, with emphasis on physics and applications in molecular optical sensing. The unique properties lead to new sensing methodologies, such as SES, imaging-based molecular detections, and chiral sensing. Both plasmonic and dielectric metasurfaces as well as their latest developments were discussed. The features of this rapidly developing research along with the obstacles and the future prospects were also outlined. As far as the fabrication processing is concerned, there is a good matching with the conventional production of metallic/semiconductor/dielectrics. Thus, metasurfaces with suitable materials and device architecture design display a very promising potential in optical sensing. The possibility to design with more freedom and to have access to a wider range of materials makes metasurfaces to be very attractive for various applications.

Conflict of Interest

The authors declare no conflict of interest.

[1] X. Fan, I. M. White, S. I. Shopova, H. Zhu, J. D. Suter, Y. Sun, *Anal. Chim. Acta* **2008**, *620*, 8.

[2] X. Yao, S. Jiang, S. Luo, B.-W. Liu, T.-X. Huang, S. Hu, J. Zhu, X. Wang, B. Ren, *ACS Appl. Mater. Interfaces* **2020**, *12*, 36505.

[3] J. Zhu, X. Chen, Y. Xie, J.-Y. Ou, H. Chen, Q. H. Liu, *Nanophotonics* **2020**, *9*, 167.

[4] J. Zhou, F. Tao, J. Zhu, S. Lin, Z. Wang, X. Wang, J.-Y. Ou, Y. Li, Q. H. Liu, *Nanophotonics* **2019**, *8*, 307.

[5] R. Ahmed, M. O. Ozen, M. G. Karaaslan, C. A. Prator, C. Thanh, S. Kumar, L. Torres, N. Iyer, S. Munter, S. Southern, *Adv. Mater.* **2020**, *32*, 1907160.

[6] Z. Li, X. Tian, C.-W. Qiu, J. S. Ho, *Nat. Electron.* **2021**, 1.

[7] P. Bouchal, P. Dvořák, J. Babocky, Z. Bouchal, F. Ligmajer, M. Hrton, V. Křápek, A. Faßbender, S. Linden, R. Chmelík, *Nano Lett.* **2019**, *19*, 1242.

[8] G. Palermo, M. Rippa, Y. Conti, A. Vestri, R. Castagna, G. Fusco, E. Suffredini, J. Zhou, J. Zyss, A. De Luca, *ACS Appl. Mater. Interfaces* **2021**, *13*, 43715.

[9] Y. Liang, H. Zhang, W. Zhu, A. Agrawal, H. Lezec, L. Li, W. Peng, Y. Zou, Y. Lu, T. Xu, *Sensors* **2017**, *2*, 1796.

[10] B. Liu, S. Chen, J. Zhang, X. Yao, J. Zhong, H. Lin, T. Huang, Z. Yang, J. Zhu, S. Liu, *Materials* **2018**, *30*, 1706031.

**ADVANCED
SCIENCE NEWS**

www.advancedsciencenews.com

**ADVANCED
OPTICAL
MATERIALS**

www.advopticalmat.de

[11] Y. Jahani, E. R. Arvelo, F. Yesilkoy, K. Koshelev, C. Cianciaruso, M. De Palma, Y. Kivshar, H. Altug, *Nat. Commun.* **2021**, *12*, 1.

[12] M. Gao, W. Yang, Z. Wang, S. Lin, J. Zhu, Z. Yang, *Photonics Res.* **2020**, *8*, 1226.

[13] Z. Zhang, H. Wang, Z. Chen, X. Wang, J. Choo, L. Chen, *Biosens. Bioelectron.* **2018**, *114*, 52.

[14] J. Cai, C. Zhang, C. Liang, S. Min, X. Cheng, W. D. Li, *Adv. Opt. Mater.* **2019**, *7*, 1900516.

[15] S. Zeng, K. V. Sreekanth, J. Shang, T. Yu, C. K. Chen, F. Yin, D. Baillargeat, P. Coquet, H. P. Ho, A. V. Kabashin, *Adv. Mater.* **2015**, *27*, 6163.

[16] M. Consales, G. Quero, S. Spaziani, M. Principe, A. Micco, V. Galdi, A. Cutolo, A. Cusano, *Laser Photonics Rev.* **2020**, *14*, 2000180.

[17] Z. Long, Y. Liang, L. Feng, H. Zhang, M. Liu, T. Xu, *Nat. Commun.* **2020**, *12*, 10809.

[18] R. H. Siddique, S. Kumar, V. Narasimhan, H. Kwon, H. Choo, *ACS Nano* **2019**, *13*, 13775.

[19] S. Chen, C. Lin, *Mater. Res. Express* **2019**, *6*, 056503.

[20] A. Danilov, G. Tselikov, F. Wu, V. G. Kravets, I. Ozerov, F. Bedu, A. N. Grigorenko, A. V. Kabashin, *Biosens. Bioelectron.* **2018**, *104*, 102.

[21] O. Tokel, F. Inci, U. Demirci, *Chem. Rev.* **2014**, *114*, 5728.

[22] J. Zhu, Z. Wang, S. Lin, S. Jiang, X. Liu, S. Guo, *Biosens. Bioelectron.* **2020**, *150*, 111905.

[23] J. Langer, D. Jimenez de Aberasturi, J. Aizpurua, R. A. Alvarez-Puebla, B. Auguié, J. J. Baumberg, G. C. Bazan, S. E. Bell, A. Boisen, A. G. Brolo, *ACS Nano* **2019**, *14*, 28.

[24] F. Neubrech, C. Huck, K. Weber, A. Pucci, H. Giessen, *Chem. Rev.* **2017**, *117*, 5110.

[25] M. C. Giordano, M. Tzschoppe, M. Barelli, J. Vogt, C. Huck, F. Canepa, A. Pucci, *ACS Appl. Mater. Interfaces* **2020**, *12*, 11155.

[26] M. Tzschoppe, C. Huck, J. Vogt, F. Neubrech, A. Pucci, *J. Phys. Chem. C* **2018**, *122*, 15678.

[27] P. J. S. Singh, a. B. Chemical, *SPR biosensors: historical perspectives and current challenges* **2016**, *229*, 110.

[28] J. Homola, *Chem. Rev.* **2008**, *108*, 462.

[29] M. Abb, Y. Wang, N. Papasimakis, C. De Groot, O. L. Muskens, *Nano Lett.* **2014**, *14*, 346.

[30] P. Albella, R. Alcaraz de la Osa, F. Moreno, S. A. Maier, *ACS Photonics* **2014**, *1*, 524.

[31] M. Caldarola, P. Albella, E. Cortés, M. Rahmani, T. Roschuk, G. Grinblat, R. F. Oulton, A. V. Bragas, S. A. Maier, *Nat. Commun.* **2015**, *6*, 1.

[32] J. Zhu, S. Jiang, Y. Xie, F. Li, L. Du, K. Meng, L. Zhu, J. Zhou, *Opt. Lett.* **2020**, *45*, 2335.

[33] S. Ding, J.-Y. Ou, L. Du, L. Zhu, S. A. Khan, H. Chen, J. Zhu, *Corban* **2021**, *179*, 666.

[34] J. González-Colsa, G. Serrera, J. M. Saiz, F. González, F. Moreno, P. Albella, *Opt. Express* **2021**, *29*, 13733.

[35] J. Kim, S. Choudhury, C. DeVault, Y. Zhao, A. V. Kildishev, V. M. Shalaev, A. Alù, A. Boltasseva, *ACS Nano* **2016**, *10*, 9326.

[36] Y. Hu, X. Wang, X. Luo, X. Ou, L. Li, Y. Chen, P. Yang, S. Wang, H. Duan, *Nanophotonics* **2020**, *9*, 3755.

[37] V. Kravets, F. Schedin, A. Grigorenko, *Physics Review Letters* **2008**, *101*, 087403.

[38] S.-Q. Li, W. Zhou, D. Bruce Buchholz, J. B. Ketterson, L. E. Ocola, K. Sakoda, R. P. Chang, *Appl. Phys. Lett.* **2014**, *104*, 231101.

[39] V. G. Kravets, A. V. Kabashin, W. L. Barnes, A. N. Grigorenko, *Chem. Rev.* **2018**, *118*, 5912.

[40] D. Khlopin, F. Laux, W. P. Wardley, J. Martin, G. A. Wurtz, J. Plain, N. Bonod, A. V. Zayats, W. Dickson, D. J. Gérard, *J. Opt. Soc. Am. B* **2017**, *34*, 691.

[41] S. Rodriguez, M. Schaafsma, A. Berrier, J. G. Rivas, *Phys. B* **2012**, *407*, 4081.

[42] Q. Le-Van, E. Zoethout, E. J. Geluk, M. Ramezani, M. Berghuis, J. Gómez Rivas, *Adv. Opt. Mater.* **2019**, *7*, 1801451.

[43] S. J. C. P. L. Oldenburg, R. D. Averitt, S. L. Westcott, N. J. Halas, *Chem. Phys. Lett.* **1998**, *288*, 243.

[44] O. Reshef, M. Saad-Bin-Alam, M. J. Huttunen, G. Carlow, B. T. Sullivan, J.-M. Ménard, K. Dolgaleva, R. W. Boyd, *Nano Lett.* **2019**, *19*, 6429.

[45] V. A. J. Markel, *J. Phys. B: At., Mol. Opt. Phys.* **2005**, *38*, L115.

[46] S. A. Maier, *Plasmonics: Fundamentals and Applications*, Springer Science & Business Media, Berlin **2007**.

[47] C. Huang, X. Yin, Y. Zhang, S. Wang, Y. Zhu, H. Liu, C. T. Chan, *Phys. Rev. B* **2012**, *85*, 235410.

[48] Y. Yang, I. I. Kravchenko, D. P. Briggs, J. Valentine, *arXiv:1405.3901*, **2014**.

[49] L. Zundel, A. J. Manjavacas, *J. Phys.: Photonics* **2018**, *1*, 015004.

[50] K. Yang, J. Wang, X. Yao, D. Lyu, J. Zhu, Z. Yang, B. Liu, B. Ren, *Adv. Opt. Mater.* **2021**, *9*, 2001375.

[51] M. S. Bin-Alam, O. Reshef, Y. Mamchur, M. Z. Alam, G. Carlow, J. Upham, B. T. Sullivan, J.-M. Ménard, M. J. Huttunen, R. W. Boyd, *Nat. Commun.* **2021**, *12*, 1.

[52] B. Auguié, W. L. Barnes, *Physics Review Letters* **2008**, *101*, 143902.

[53] N. Meinzer, W. L. Barnes, I. R. Hooper, *Nat. Photonics* **2014**, *8*, 889.

[54] A. Lahav, M. Auslender, I. Abdulhalim, *Opt. Lett.* **2008**, *33*, 2539.

[55] S. Shukla, N. K. Sharma, V. Sajal, *Sens. Actuators, B* **2015**, *206*, 463.

[56] M. Bao, G. Li, D. Jiang, W. Cheng, X. Ma, *Appl. Phys. A* **2012**, *107*, 279.

[57] F. Benkabou, M. Chikhi, *Phys. Status Solidi* **2014**, *211*, 700.

[58] J. Zhou, T. Koschny, L. Zhang, G. Tuttle, C. M. Soukoulis, *Appl. Phys. Lett.* **2006**, *88*, 221103.

[59] J. B. Pendry, A. Holden, W. Stewart, I. Youngs, *Physics Review Letters* **1996**, *76*, 4773.

[60] D. R. Smith, W. J. Padilla, D. Vier, S. C. Nemat-Nasser, S. Schultz, *Physics Review Letters* **2000**, *84*, 4184.

[61] C. Cen, Z. Chen, D. Xu, L. Jiang, X. Chen, Z. Yi, P. Wu, G. Li, Y. Yi, *Nanomaterials* **2020**, *10*, 95.

[62] M. A. Butt, N. L. Kazansky, *Photonics Lett. Pol.* **2020**, *12*, 88.

[63] A. Patoux, G. Agez, C. Girard, V. Paillard, P. R. Wiecha, A. Lecestre, F. Carcenac, G. Larrieu, A. Arbouet, *Sci. Rep.* **2021**, *11*, 1.

[64] N. Yu, F. Capasso, *Nat. Mater.* **2014**, *13*, 139.

[65] X. Luo, *Adv. Opt. Mater.* **2018**, *6*, 1701201.

[66] J. Hu, S. Bandyopadhyay, Y.-H. Liu, L.-Y. Shao, *Front. Phys.* **2021**, *8*, 502.

[67] N. L. Kazanskiy, M. A. Butt, S. N. Khonina, *Sensors* **2021**, *21*, 378.

[68] J. Ding, N. Xu, H. Ren, Y. Lin, W. Zhang, H. Zhang, *Sci. Rep.* **2016**, *6*, 1.

[69] S. Zhang, C. L. Wong, S. Zeng, R. Bi, K. Tai, K. Dholakia, M. Olivo, *Nanophotonics* **2021**, *10*, 259.

[70] A. Leitis, A. Tittl, M. Liu, B. H. Lee, M. B. Gu, Y. S. Kivshar, H. Altug, *Sci. Adv.* **2019**, *5*, eaaw2871.

[71] A. Tittl, A. Leitis, M. Liu, F. Yesilkoy, D.-Y. Choi, D. N. Neshev, Y. S. Kivshar, H. Altug, *Sci. Adv.* **2018**, *360*, 1105.

[72] G. Palermo, K. V. Sreekanth, N. Maccaferri, G. E. Lio, G. Nicoletta, F. De Angelis, M. Hinczewski, G. Strangi, *Nanophotonics* **2021**, *10*, 295.

[73] Y. Zhu, Z. Li, Z. Hao, C. DiMarco, P. Maturavongsadit, Y. Hao, M. Lu, A. Stein, Q. Wang, J. J. L. S. Hone, *Light: Sci. Appl.* **2018**, *7*, 1.

[74] J. He, T. Dong, B. Chi, Y. Zhang, *J. Infrared, Millimeter, Terahertz Waves* **2020**, *41*, 607.

[75] Q. Jiang, G. Jin, L. Cao, *Adv. Opt. Photonics* **2019**, *11*, 518.

[76] B. Shuai, L. Xia, D. Liu, *Opt. Express* **2012**, *20*, 25858.

[77] A. R. Tao, *Nat. Photonics* **2014**, *8*, 6.

[78] S.-C. Huang, X. Wang, Q.-Q. Zhao, J.-F. Zhu, C.-W. Li, Y.-H. He, S. Hu, M. M. Sartin, S. Yan, B. Ren, *Nat. Commun.* **2020**, *11*, 1.

[79] J. N. Anker, W. P. Hall, O. Lyandres, N. C. Shah, J. Zhao, D. Van, *Nat. Mater.* **2008**, *7*, 308.

**ADVANCED
SCIENCE NEWS**

www.advancedsciencenews.com

**ADVANCED
OPTICAL
MATERIALS**

www.advopticalmat.de

[80] S. I. Azzam, A. V. Kildishev, R.-M. Ma, C.-Z. Ning, R. Oulton, V. M. Shalaev, M. I. Stockman, J.-L. Xu, X. Applications Zhang, *Light: Sci. Appl.* **2020**, *9*, 1.

[81] M. Ren, B. Jia, J. Y. Ou, E. Plum, J. Zhang, K. F. MacDonald, A. E. Nikolaenko, J. Xu, M. Gu, N. I. Zheludev, *Adv. Mater.* **2011**, *23*, 5540.

[82] N. Yu, P. Genevet, M. A. Kats, F. Aieta, J.-P. Tetienne, F. Capasso, Z. Gaburro, *Sci. Adv.* **2011**, *334*, 333.

[83] R. Won, *Nat. Photonics* **2017**, *11*, 462.

[84] R. W. Boyd, *Nonlinear Optics*, Academic Press, Cambridge, MA **2020**.

[85] S. Oldenburg, R. Averitt, S. Westcott, N. Halas, *Chem. Phys. Lett.* **1998**, *288*, 243.

[86] M. Kauranen, A. V. Zayats, *Nat. Photonics* **2012**, *6*, 737.

[87] F. Jiao, F. Li, J. Shen, C. Guan, S. A. Khan, J. Wang, Z. Yang, J. Zhu, *Sens. Actuators, B* **2021**, *344*, 130170.

[88] L. Novotny, N. Van Hulst, *Nat. Photonics* **2011**, *5*, 83.

[89] X. Zhang, H. S. Choi, A. M. Armani, *Appl. Phys. Lett.* **2010**, *96*, 153304.

[90] X. Ji, F. A. Barbosa, S. P. Roberts, A. Dutt, J. Cardenas, Y. Okawachi, A. Bryant, A. L. Gaeta, M. Lipson, *Optica* **2017**, *4*, 619.

[91] T. Asano, Y. Ochi, Y. Takahashi, K. Kishimoto, S. Noda, *Opt. Express* **2017**, *25*, 1769.

[92] M. Kauranen, A. Zayats, *Nat. Photonics* **2012**, *6*, 737.

[93] A. Krasnok, M. Tymchenko, A. Alù, *Mater. Today* **2018**, *21*, 8.

[94] M. Celebrano, X. Wu, M. Baselli, S. Großmann, P. Biagioni, A. Locatelli, C. De Angelis, G. Cerullo, R. Osellame, B. Hecht, *Nat. Nanotechnol.* **2015**, *10*, 412.

[95] B. Sain, C. Meier, T. Zentgraf, *Adv. Photonics* **2019**, *1*, 024002.

[96] K. Koshelev, S. Kruk, E. Melik-Gaykazyan, J.-H. Choi, A. Bogdanov, H.-G. Park, Y. Kivshar, *Science* **2020**, *367*, 288.

[97] P. Nordlander, C. Oubre, E. Prodan, K. Li, M. Stockman, *Nano Lett.* **2004**, *4*, 899.

[98] Y. Chu, E. Schonbrun, T. Yang, K. B. Crozier, *Appl. Phys. Lett.* **2008**, *93*, 181108.

[99] G. Dayal, X. Y. Chin, C. Soci, R. Singh, *Adv. Opt. Mater.* **2017**, *5*, 1600559.

[100] L. Liu, Z. Li, C. Cai, W. Zhu, X. Zheng, W. Zhang, J. Xu, Z. Liu, *Appl. Phys. Lett.* **2020**, *117*, 081108.

[101] S. Zou, N. Janel, G. C. J. T. Schatz, *J. Chem. Phys.* **2004**, *120*, 10871.

[102] V. I. Zakomirnyi, I. L. Rasskazov, V. S. Gerasimov, A. E. Ershov, S. P. Polyutov, S. V. Karpov, *Appl. Phys. Lett.* **2017**, *111*, 123107.

[103] S. Deng, R. Li, J.-E. Park, J. Guan, P. Choo, J. Hu, P. J. Smeets, T. W. Odom, *Proc. Natl. Acad. Sci. U. S. A.* **2020**, *117*, 23380.

[104] B. Auguié, X. M. Bendana, W. L. Barnes, F. J. G. de Abajo, *Phys. Rev. B* **2010**, *82*, 155447.

[105] C.-P. Huang, X.-G. Yin, H. Huang, Y.-Y. Zhu, *Opt. Express* **2009**, *17*, 6407.

[106] F. Yue, C. Zhang, X.-F. Zang, D. Wen, B. D. Gerardot, S. Zhang, X. Chen, *Light: Sci. Appl.* **2018**, *7*, 17129.

[107] G.-Y. Lee, G. Yoon, S.-Y. Lee, H. Yun, J. Cho, K. Lee, H. Kim, J. Rho, B. Lee, *Nanoscale* **2018**, *10*, 4237.

[108] S. Colburn, A. Zhan, A. Majumdar, *Sci. Adv.* **2018**, *4*, eaar2114.

[109] W. T. Chen, A. Y. Zhu, V. Sanjeev, M. Khorasaninejad, Z. Shi, E. Lee, F. Capasso, *Nat. Nanotechnol.* **2018**, *13*, 220.

[110] G. Zheng, H. Mühlenbernd, M. Kenney, G. Li, T. Zentgraf, S. Zhang, *Nat. Nanotechnol.* **2015**, *10*, 308.

[111] H. Yang, G. Li, G. Cao, Z. Zhao, J. Chen, K. Ou, X. Chen, W. Lu, *Opt. Express* **2018**, *26*, 5632.

[112] M. Khorasaninejad, F. Capasso, *Science* **2017**, *358*, eaam8100.

[113] W. T. Chen, A. Y. Zhu, M. Khorasaninejad, Z. Shi, V. Sanjeev, F. Capasso, *Nano Lett.* **2017**, *17*, 3188.

[114] M. Khorasaninejad, W. T. Chen, R. C. Devlin, J. Oh, A. Y. Zhu, F. Capasso, *Science* **2016**, *352*, 1190.

[115] S. J. Byrnes, A. Lenef, F. Aieta, F. Capasso, *Opt. Express* **2016**, *24*, 5110.

[116] E. Arbabi, A. Arbabi, S. M. Kamali, Y. Horie, A. Faraon, *Optica* **2016**, *3*, 628.

[117] A. Arbabi, Y. Horie, A. J. Ball, M. Bagheri, A. Faraon, *Nat. Commun.* **2015**, *6*, 7069.

[118] H.-T. Chen, A. J. Taylor, N. Yu, *Rep. Prog. Phys.* **2016**, *79*, 076401.

[119] A. V. Kildishev, A. Boltasseva, V. M. Shalaev, *Science* **2013**, *339*, 1232009.

[120] A. E. Minovich, A. E. Miroshnichenko, A. Y. Bykov, T. V. Murzina, D. N. Neshev, Y. S. Kivshar, *Laser Photonics Rev.* **2015**, *9*, 195.

[121] C.-C. Chang, W. J. Kort-Kamp, J. Nogan, T. S. Luk, A. K. Azad, A. J. Taylor, D. A. Dalvit, M. Sykora, H.-T. Chen, *Nano Lett.* **2018**, *18*, 7665.

[122] T. D. Dao, S. Ishii, T. Yokoyama, T. Sawada, R. P. Sugavaneshwar, K. Chen, Y. Wada, T. Nabatame, T. Nagao, *ACS Photonics* **2016**, *3*, 1271.

[123] Z.-g. Dai, X.-h. Xiao, W. Wu, Y.-p. Zhang, L. Liao, S.-s. Guo, J.-j. Ying, C.-x. Shan, M.-t. Sun, C.-z. Jiang, *Light: Sci. Appl.* **2015**, *4*, e342.

[124] W. Li, J. Valentine, *Nano Lett.* **2014**, *14*, 3510.

[125] H.-H. Chen, Y.-C. Su, W.-L. Huang, C.-Y. Kuo, W.-C. Tian, M.-J. Chen, S.-C. Lee, *Appl. Phys. Lett.* **2014**, *105*, 023109.

[126] S. Cao, W. Yu, T. Wang, Z. Xu, C. Wang, Y. Fu, Y. Liu, *Appl. Phys. Lett.* **2013**, *102*, 161109.

[127] J. Hao, J. Wang, X. Liu, W. J. Padilla, L. Zhou, M. Qiu, *Appl. Phys. Lett.* **2010**, *96*, 251104.

[128] Y. Kivshar, *Natl. Sci. Rev.* **2018**, *5*, 144.

[129] S. Kruk, Y. Kivshar, *ACS Photonics* **2017**, *4*, 2638.

[130] M. Decker, I. J. Staude, *J. Opt.* **2016**, *18*, 103001.

[131] M. Decker, I. Staude, M. Falkner, J. Dominguez, D. N. Neshev, I. Brener, T. Pertsch, Y. S. Kivshar, *Adv. Opt. Mater.* **2015**, *3*, 813.

[132] J. Cheng, D. Ansari-Oghol-Beig, H. Mosallaei, *Opt. Lett.* **2014**, *39*, 6285.

[133] I. Staude, A. E. Miroshnichenko, M. Decker, N. T. Fofang, S. Liu, E. Gonzales, J. Dominguez, T. S. Luk, D. N. Neshev, *ACS Nano* **2013**, *7*, 7824.

[134] A. B. Evlyukhin, C. Reinhardt, B. N. Chichkov, *Phys. Rev. B* **2011**, *84*, 235429.

[135] K. He, S. Xiao, J. J. I. Zhu, *IEEE B Journal of Selected Topic* **2021**, *27*, 1.

[136] M. Kerker, D.-S. Wang, C. Giles, *J. Opt. Soc. Am.* **1983**, *73*, 765.

[137] A. Barreda, J. Saiz, F. González, F. Moreno, P. Albella, *AIP Adv.* **2019**, *9*, 040701.

[138] A. B. Evlyukhin, C. Reinhardt, A. Seidel, B. S. Luk'yanchuk, B. N. Chichkov, *Phys. Rev. B* **2010**, *82*, 045404.

[139] A. García-Etxarri, R. Gómez-Medina, L. S. Froufe-Pérez, C. López, L. Chantada, F. Scheffold, J. Aizpurua, M. Nieto-Vesperinas, J. J. Sáenz, *Opt. Express* **2011**, *19*, 4815.

[140] P. Albella, M. A. Poyli, M. K. Schmidt, S. A. Maier, F. Moreno, J. J. Sáenz, J. Aizpurua, *J. Phys. Chem. C* **2013**, *117*, 13573.

[141] A. I. Barreda, H. Saleh, A. Litman, F. González, J.-M. Geffrin, F. Moreno, *Nat. Commun.* **2017**, *8*, 1.

[142] T. Shibanuma, T. Matsui, T. Roschuk, J. Wojcik, P. Mascher, P. Albella, S. A. Maier, *ACS Photonics* **2017**, *4*, 489.

[143] D. G. Baranov, S. V. Makarov, A. E. Krasnok, P. A. Belov, A. Alù, *Laser Photonics Rev.* **2016**, *10*, 1009.

[144] B. S. Luk'yanchuk, N. V. Voshchinnikov, R. Paniagua-Domínguez, A. Kuznetsov, *ACS Photonics* **2015**, *2*, 993.

[145] J. Yan, P. Liu, Z. Lin, H. Wang, H. Chen, C. Wang, G. Yang, *ACS Nano* **2015**, *9*, 2968.

[146] T. Shibanuma, P. Albella, S. A. Maier, *Nanoscale* **2016**, *8*, 14184.

[147] W. Liu, J. Zhang, B. Lei, H. Ma, W. Xie, H. Hu, *Opt. Express* **2014**, *22*, 16178.

**ADVANCED
SCIENCE NEWS**

www.advancedsciencenews.com

**ADVANCED
OPTICAL
MATERIALS**

www.advopticalmat.de

[148] J. Li, N. Verellen, D. Vercruysse, T. Bearda, L. Lagae, P. Van Dorpe, *Nano Lett.* **2016**, *16*, 4396.

[149] S. Murai, G. W. Castellanos, T. Raziman, A. G. Curto, J. G. Rivas, *Adv. Opt. Mater.* **2020**, *8*, 1902024.

[150] C. F. Bohren, D. R. Huffman, *Absorption and Scattering of Light by Small Particles*, John Wiley & Sons, Hoboken, NJ **2008**.

[151] L. Cao, P. Fan, E. S. Barnard, A. M. Brown, M. L. Brongersma, *Nano Lett.* **2010**, *10*, 2649.

[152] A. I. Kuznetsov, A. E. Miroshnichenko, Y. H. Fu, J. Zhang, B. Luk'yanchuk, *Sci. Rep.* **2012**, *2*, 492.

[153] M. Semmlinger, M. L. Tseng, J. Yang, M. Zhang, C. Zhang, W.-Y. Tsai, D. P. Tsai, P. Nordlander, N. J. Halas, *Nano Lett.* **2018**, *18*, 5738.

[154] J. C. Ginn, I. Brener, D. W. Peters, J. R. Wendt, J. O. Stevens, P. F. Hines, L. I. Basilio, L. K. Warne, J. F. Ihlefeld, P. G. Clem, *Physics Review Letters* **2012**, *108*, 097402.

[155] M. R. Shcherbakov, D. N. Neshev, B. Hopkins, A. S. Shorokhov, I. Staude, E. V. Melik-Gaykazyan, M. Decker, A. A. Ezhov, A. E. Miroshnichenko, *Nano Lett.* **2014**, *14*, 6488.

[156] A. Vázquez-Guardado, D. Chanda, *Physics Review Letters* **2018**, *120*, 137601.

[157] J. Jeong, M. D. Goldflam, S. Campione, J. L. Briscoe, P. P. Vabishchevich, J. Nogan, M. B. Sinclair, T. S. Luk, I. Brener, *ACS Photonics* **2020**, *7*, 1699.

[158] S. Yuan, X. Qiu, C. Cui, L. Zhu, Y. Wang, Y. Li, J. Song, Q. Huang, J. Xia, *ACS Nano* **2017**, *11*, 10704.

[159] K. Koshelev, S. Lepeshov, M. Liu, A. Bogdanov, Y. Kivshar, *Phys. Rev. Lett.* **2018**, *121*, 193903.

[160] K. Koshelev, Y. Kivshar, *Light trapping gets a boost*, Nature Publishing Group, **2019**.

[161] C. W. Hsu, B. Zhen, A. D. Stone, J. D. Joannopoulos, M. Soljačić, *Nat. Rev. Mater.* **2016**, *1*, 16048.

[162] N. Muhammad, Y. Chen, C.-W. Qiu, G. P. Wang, *Nano Lett.* **2021**, *21*, 967.

[163] M. E. Germain, M. J. Knapp, *Chem. Soc. Rev.* **2009**, *38*, 2543.

[164] F. Long, A. Zhu, H. Shi, *Sensors* **2013**, *13*, 13928.

[165] F. B. Myers, L. P. Lee, *Lab Chip* **2008**, *8*, 2015.

[166] L. Huang, X. Chen, H. Mühlenbernd, H. Zhang, S. Chen, B. Bai, Q. Tan, G. Jin, K.-W. Cheah, C.-W. Qiu, J. Li, T. Zentgraf, S. Zhang, *Nat. Commun.* **2013**, *4*, 2808.

[167] A. M. Shaltout, K. G. Lagoudakis, J. van de Groep, S. J. Kim, J. Vučković, V. M. Shalaev, M. L. Brongersma, *Science* **2019**, *365*, 374.

[168] S. Chen, W. Liu, Z. Li, H. Cheng, J. Tian, *Adv. Mater.* **2020**, *32*, 1805912.

[169] Y. Yang, I. I. Kravchenko, D. P. Briggs, J. Valentine, *Nat. Commun.* **2014**, *5*, 5753.

[170] Y. Chang, D. Hasan, B. Dong, J. Wei, Y. Ma, G. Zhou, K. W. Ang, C. Lee, *ACS Appl. Mater. Interfaces* **2018**, *10*, 38272.

[171] P. H. Rogers, G. Sirinakis, M. A. J. T. Carpenter, *J. Phys. Chem. C* **2008**, *112*, 6749.

[172] S. Lee, K. Lee, J. Ahn, J. Lee, M. Kim, Y. Shin, *ACS Nano* **2011**, *5*, 897.

[173] J. Bian, X. Xing, S. Zhou, Z. Man, Z. Lu, W. Zhang, *Nanoscale* **2019**, *11*, 12471.

[174] F. Yesilkoy, E. R. Arvelo, Y. Jahani, M. Liu, A. Tittl, V. Cevher, Y. Kivshar, H. J. N. P. Altug, *Nat. Photonics* **2019**, *13*, 390.

[175] A. Tittl, A. John-Herpin, A. Leitis, E. R. Arvelo, H. Altug, *Angew. Chem.* **2019**, *58*, 14810.

[176] S. Min, S. Li, Z. Zhu, Y. Liu, C. Liang, J. Cai, F. Han, Y. Li, W. Cai, X. Cheng, *Adv. Mater.* **2021**, *33*, 2100270.

[177] R. Adato, A. A. Yanik, J. J. Amsden, D. L. Kaplan, F. G. Omenetto, M. K. Hong, S. Erramilli, H. Altug, *Proc. Natl. Acad. Sci. U. S. A.* **2009**, *106*, 19227.

[178] L. Dong, X. Yang, C. Zhang, B. Cerjan, L. Zhou, M. L. Tseng, Y. Zhang, A. Alabastri, P. Nordlander, N. J. Halas, *Nano Lett.* **2017**, *17*, 5768.

[179] X. Gai, D.-Y. Choi, B. Luther-Davies, *Opt. Express* **2014**, *22*, 9948.

[180] A. Arbabi, Y. Horie, M. Bagheri, A. Faraon, *Nat. Nanotechnol.* **2015**, *10*, 937.

[181] S. Campione, S. Liu, L. I. Basilio, L. K. Warne, W. L. Langston, T. S. Luk, J. R. Wendt, J. L. Reno, G. A. Keeler, *ACS Photonics* **2016**, *3*, 2362.

[182] Q. Wang, E. T. Rogers, B. Gholipour, C.-M. Wang, G. Yuan, J. Teng, N. I. Zheludev, *Nat. Photonics* **2016**, *10*, 60.

[183] P. Wang, M. E. Nasir, A. V. Krasavin, W. Dickson, Y. Jiang, A. V. Zayats, *Acc. Chem. Res.* **2019**, *52*, 3018.

[184] C. Zong, M. Xu, L.-J. Xu, T. Wei, X. Ma, X.-S. Zheng, R. Hu, B. Ren, *Chem. Rev.* **2018**, *118*, 4946.

[185] J. A. Dieringer, R. B. Lettan, K. A. Scheidt, R. P. J. Van Duyne, *J. Am. Chem. Soc.* **2007**, *129*, 16249.

[186] D. Rodrigo, A. Tittl, N. Ait-Bouziad, A. John-Herpin, O. Limaj, C. Kelly, D. Yoo, N. J. Wittenberg, S.-H. Oh, H. A. Lashuel, *Nat. Commun.* **2018**, *9*, 2160.

[187] R. Zvagelsky, D. Chubich, A. Pisarenko, Z. Bedran, E. Zhukova, *J. Phys. Chem. C* **2021**, *125*, 4694.

[188] J. Vogt, C. Huck, F. Neubrech, A. Toma, D. Gerbert, A. Pucci, *Phys. Chem. Chem. Phys.* **2015**, *17*, 21169.

[189] M. Rybin, Y. J. N. Kivshar, *Nature* **2017**, *541*, 164.

[190] S. Romano, G. Zito, S. Managò, G. Calafiore, E. Penzo, S. Cabrini, A. C. De Luca, V. J. T. Mocella, *J. Phys. Chem., C* **2018**, *122*, 19738.

[191] S. Romano, G. Zito, S. Torino, G. Calafiore, E. Penzo, G. Coppola, S. Cabrini, I. Rendina, V. Mocella, *Photonics Res.* **2018**, *6*, 726.

[192] S. Romano, A. Lamberti, M. Masullo, E. Penzo, S. Cabrini, I. Rendina, V. Mocella, *Mater. Today* **2018**, *11*, 526.

[193] F. B. Barho, F. Gonzalez-Posada, M. Bomers, A. Mezy, L. Cerutti, T. Taliercio, *ACS Photonics* **2019**, *6*, 1506.

[194] J.-J. Greffet, R. Carminati, K. Joulain, J.-P. Mulet, S. Mainguy, Y. Chen, *Nature* **2002**, *416*, 61.

[195] F. Marquier, K. Joulain, J.-P. Mulet, R. Carminati, J.-J. Greffet, Y. Chen, *Phys. Rev. B* **2004**, *69*, 155412.

[196] J. Kumar, H. Eraña, E. López-Martínez, N. Claes, V. F. Martín, D. M. Solís, S. Bals, A. L. Cortajarena, J. Castilla, L. M. Liz-Marzán, *Proc. Natl. Acad. Sci. U. S. A.* **2018**, *115*, 3225.

[197] G. Li, K. DeLaney, L. Li, *Nat. Commun.* **2019**, *10*, 5038.

[198] M. Li, S. E. Howson, K. Dong, N. Gao, J. Ren, P. Scott, X. J. Qu, *J. Am. Chem. Soc.* **2014**, *136*, 11655.

[199] H. Haken, H. C. Wolf, *Molecular Physics and Elements of Quantum Chemistry: Introduction to Experiments and Theory*, Springer Science & Business Media, Berlin **2013**.

[200] A. Rodger, B. Nordén, *Circular Dichroism and Linear Dichroism*, Vol. *1*, Oxford University Press, Oxford **1997**.

[201] N. Berova, K. Nakanishi, R. W. Woody, *Circular Dichroism: Principles and Applications*, John Wiley & Sons, Hoboken, NJ **2000**.

[202] E. Mohammadi, K. Tsakmakidis, A. N. Askarpour, P. Dehkhoda, A. Tavakoli, H. Altug, *ACS Photonics* **2018**, *5*, 2669.

[203] G. Serrera, J. González-Colsa, V. Giannini, J. M. Saiz, P. Albella, R. Transfer, *J. Quant. Spectrosc. Radiat. Transfer* **2022**, *284*, 108166.

[204] F. R. Gómez, O. N. OliveiraJr, P. Albella, J. Mejía-Salazar, *Phys. Rev. B* **2020**, *101*, 155403.

[205] G. Palermo, G. E. Lio, M. Esposito, L. Ricciardi, M. Manoccio, V. Tasco, A. Passaseo, A. De Luca, G. Strangi, *ACS Appl. Mater. Interfaces* **2020**, *12*, 30181.

[206] F. Koohyar, F. Kiani, S. Sharifi, M. Sharifirad, S. H. J. R. Rahmanpour, *Res. J. Appl. Sci., Eng. Technol.* **2012**, *4*, 3095.

[207] S. Droulias, L. Bougas, *Nano Lett.* **2020**, *20*, 5960.

[208] F. Yesilkoy, E. R. Arvelo, Y. Jahani, M. Liu, A. Tittl, V. Cevher, Y. Kivshar, H. Altug, *Nat. Photonics* **2019**, *13*, 390.

[209] S. Min, S. Li, Z. Zhu, Y. Liu, C. Liang, J. Cai, F. Han, Y. Li, W. Cai, X. Cheng, *Adv. Mater.* **2021**, *33*, 2100270.

[210] M. Runowski, S. Sobczak, J. Marciniak, I. Bukalska, S. Lis, A. Katrusiak, *Nanoscale* **2019**, *11*, 8718.

Sayed Ali Khan was born in Swabi, KPK Pakistan. He received his Master's degree in Physics (2014) from Abdul Wali Khan University, Mardan, Pakistan. He received his Ph.D. in Materials Science and Engineering (2017) from the University of Science and Technology of China under the supervision of Professor Xin Xu. From January 2018 to December 2019, he was a Postdoctoral Fellow in the Department of Microscale Optoelectronics, Shenzhen University. To date, he has been with Xiamen University, Xiamen, Fujian, China, involved in research on luminescent materials for white LEDs. Recently, he was selected as a visiting scholar at Rutgers, the State University of New Jersey, USA. He has published 60 papers and 1 book chapter in an international peer-reviewed journal as an author and a coauthor. His current research focuses on the development of broadly tunable luminescent materials for white LEDs and displays.

Jinfeng Zhu received his B.S. degree in electronic communication science and technology and his Ph.D. degree in physical electronics from the University of Electronic Science and Technology of China, Chengdu, Sichuan, China, in 2006 and 2012, respectively. From November 2009 to November 2011, he was a visiting Ph.D. student in the Department of Electrical Engineering, University of California, Los Angeles, CA, USA. From July 2017 to July 2018, he was a visiting professor at the Optoelectronics Research Centre, University of Southampton, Hampshire, UK. Since July 2012, he has been with Xiamen University, Xiamen, Fujian, China, where he is currently the Associate Dean and Professor in the Institute of Electromagnetics and Acoustics. He has authored and co-authored more than 60 peer-reviewed journal papers. His research interests include nanoantennas, nanophotonics, plasmonics, metamaterials, van der Waals materials, and related sensing applications. He is a Senior Member of the IEEE and serves as the Topic Editor of Sensors and Associate Editor of Frontiers in Materials.